Engineering Structures 323 (2025) 119253

Contents lists available at ScienceDirect

Engineering Structures

journal homepage: www.elsevier.com/locate/engstruct

Experimental characterization of prefabricated link slabs with randomly oriented and oriented-fibres UHPC under multiple geometric configurations

Junqing Xue [a,b,c], Shengrong Mao [a], Wei Xu [a], Angelo Aloisio [d,*], Yang Zhengxian [a,b,c], Alessandro Contento [a,b,c], Bruno Briseghella [a,b,c]

[a] *College of Civil Engineering, Fuzhou University, Fuzhou, China*
[b] *Fujian Provincial Key Laboratory on Multi-disasters Prevention and Mitigation in Civil Engineering, Fuzhou University, Fuzhou, China*
[c] *Joint International Research Laboratory of Deterioration and Control of Coastal and Marine Infrastructures and Materials, College of Civil Engineering, Fuzhou University, Fuzhou, China*
[d] *Department of Civil, Construction-Architectural and Environmental Engineering, Università degli Studi dell'Aquila, L'Aquila, Italy*

ARTICLE INFO

Keywords:
Ultra-High Performance Concrete (UHPC)
Link slabs
Structural
Durability
Prefabricated bridge elements
Fibre reinforcement orientation

ABSTRACT

The link slabs are structural elements connecting two bridge decks, ensuring structural continuity without altering the simple support scheme of the deck. These elements provide the durability benefits of integral bridges by eliminating expansion joints between beams, which are prone to water infiltration and exposure to degrading agents. The development of link slabs is closely connected to the progress in composite materials. Ultra-High Performance Concrete (UHPC) is a cementitious material capable of ensuring the mechanical performance of link slabs under operational loads, thanks to high resistance and durability. This work presents an extensive experimental characterization of prefabricated link slabs, considering an experimental setup representative of operational conditions. The authors examined nine experimental configurations, varying both the geometry and the material. For geometry, they varied the bolts' edge distance and the thickness of the unbonded layer. For material, they studied link slabs made of Reinforced Concrete (RC), UHPC with randomly oriented fibres, and UHPC with oriented fibres. The effect of the volumetric fraction of fibres was assessed in the slabs with oriented fibres. The results provide practical recommendations for selecting the combination of geometric properties and materials to maximize the mechanical performance of prefabricated UHPC link slabs.

1. Introduction

Expansion joints, commonly incorporated into bridge superstructures, primarily mitigate strains and stresses resulting from temperature variations. Despite their widespread application in current design and construction practices, expansion joints are often responsible for allowing water and harmful agents to seep into underlying bridge components like girders and piers, thereby accelerating structural decay [1–4]. Additionally, the need for regular maintenance due to debris accumulation further limits their functionality.

Common damages in expansion joints are shown in Fig. 1. According to a 2009 study on 71 bridges in Portugal, 91.3% of expansion joints exhibited cracks [5]; a 2011 survey in a Chinese province showed an 87.5% defect in expansion joints of 614 bridges, with 46.6% of them experiencing leaks [6].

Given such issues, jointless bridges have been considered a possible alternative to eliminate the long-term consequences of expansion joints [7,8]. Pioneering research in this area includes the work of Zuk et al. [9], who explored jointless bridges and emphasized the need for jointless abutments and flexible piers to minimize the reliance on expansion joints. Loveall [10] and Wasserman [11] proposed practical details for constructing jointless bridges. Oesterle et al. [12] suggested the elimination of expansion joints through the use of continuous precast prestressed girders. Several scholars examined semi-jointless and jointless bridges, outlining pros and cons [13–20].

In jointless bridges, link slabs are becoming increasingly widespread, particularly because they allow girders underneath to behave as simply supported structural elements. Early research in this field by Gastal and Zia [21] involved numerical modelling in assessing the performance of jointless bridges with link slabs. Zia et al. [22] expanded this research by exploring the feasibility of a debonded area where the link slab behaves independently from the bridge girders. Caner and Zia [23] conducted pioneering experimental tests on link

---

* Corresponding author.

E-mail addresses: junqing.xue@fzu.edu.cn (J. Xue), shengrong.mao@foxmail.com (S. Mao), xuwei-1017@foxmail.com (W. Xu), angelo.aloisio1@univaq.it (A. Aloisio), zxyang@fzu.edu.cn (Y. Zhengxian), alessandro@fzu.edu.cn (A. Contento), bruno@fzu.edu.cn (B. Briseghella).

https://doi.org/10.1016/j.engstruct.2024.119253
Received 29 May 2024; Received in revised form 27 September 2024; Accepted 29 October 2024

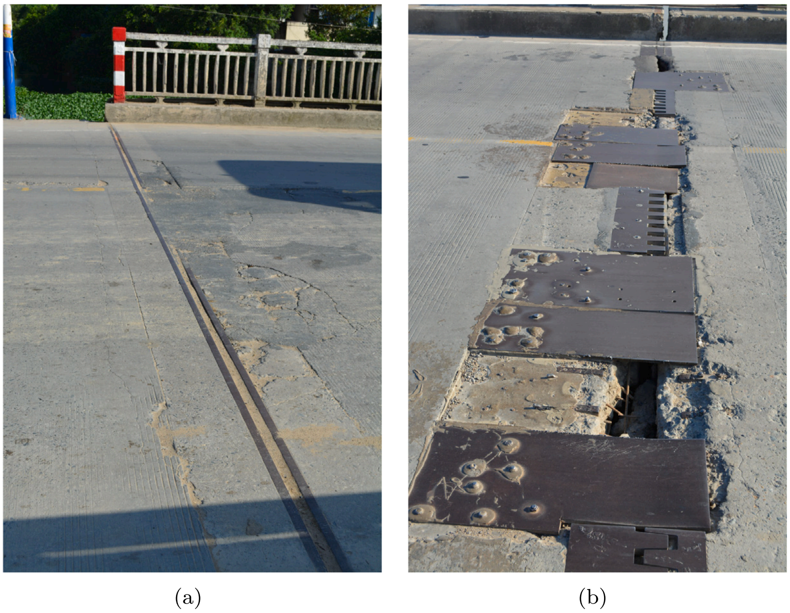
(a) (b)

Fig. 1. Illustrations of common damages in expansion joints.

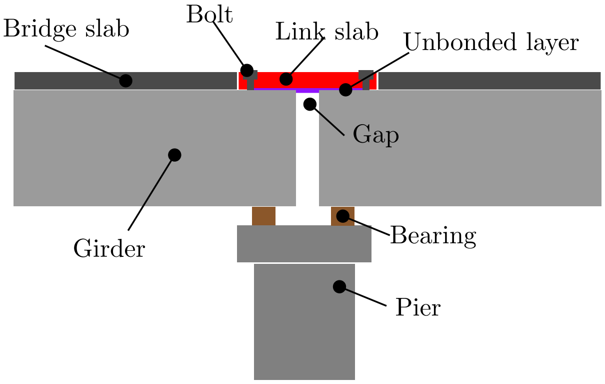

Fig. 2. Main elements of a bridge with link slab.

slabs using traditional concrete and steel rebars, which led to the development of simple design equations. Therefore, the link slab permits to combine the design and construction advantages of simply supported bridges with the durability benefits of jointless bridges [24,25], as illustrated in Fig. 2. Additionally, this solution ensures smoother vehicle rides.

The link slab, placed between two consecutive bridge spans, is subject to complex stresses originating from thermal expansion, live loads, and uneven support deformations, as shown in Fig. 2. Compared to the main beams, its relatively lower stiffness can result in stress concentration. Overlooking detailed analysis of link slabs during the design phase, along with construction quality issues and the inherently low tensile strength of RC, frequently leads to cracking and spalling in RC link slabs [26]. A survey covering 105 continuous deck bridges in the USA revealed that besides link slab cracking, other aspects generally performed well [27]. Additionally, an investigation of 75 bridges identified damage of varying degrees in 26.7% of link slabs [28].

Wing and Kowalsky [29] observed extensive cracking in the debonded region of a link slab built according to Caner and Zia's guidelines. Addressing these cracks, Li et al. [30] studied the replacement of conventional concrete in link slabs with engineered cementitious composite (ECC). Later, both Lepech and Li [31] and Samani [32] validated the effectiveness of ECC link slabs in reducing cracks. The main solution for improving the structural performance of link slabs is the exploration of alternative cementitious materials [30,33–41], such as Latex modified concrete (LMC); fibre reinforced concrete (FRC); Hybrid fibre-reinforced concrete (HyFRC) with steel and synthetic fibres; Engineering cementitious composite (ECC); Ultra-High Performance Concrete (UHPC) [42–53].

Some scholars also attempted to improve the mechanical performance of link slabs by adopting fibre-reinforced polymer (FRP) products [13,54–59]. Reyes and Robertson [60] explored the use of glass fibre-reinforced polymer (GFRP) rebars, finding that while cracks were localized, they generally remained small. Lárusson [61] also investigated link slabs with GFRP rebars under axial loads, confirming the design's ductility.

Regarding the material selection, among the different options, UHPC link slabs showed promising results thanks to their excellent mechanical performance. Specifically, their superior mechanical performance is primarily due to the material's exceptional properties, including high compressive and tensile strength, durability, and resistance to environmental impacts such as freeze-thaw cycles and corrosion [62,63]. Additionally, aligning fibres in the direction of principal stresses (typically along the length of the link slab) enhances the material's ability to resist bending and tensile forces. The dense matrix of UHPC, combined with the oriented fibres, plays a crucial role in controlling crack widths and propagation. This prevents the formation of large cracks, even under significant mechanical stresses, thereby enhancing the overall durability of the bridge.

New York's Department of Transportation successfully implemented its first UHPC link slab, which exhibited no visible cracks [64]. The enhanced performance of UHPC is attributed to fibre incorporation, with its mechanical properties being largely influenced by the orientation and distribution of these fibres [65,66]. Properly aligning fibres along the tensile stress direction boosts UHPC's tensile strength and crack resistance while optimizing fibre usage and cutting costs. Studies have shown marked improvements in UHPC's axial and flexural tensile strengths and fracture energy with oriented fibres [67,68].

Nonetheless, challenges in on-site construction and the necessity of steam curing for UHPC remain obstacles for on-site poured link slabs [69]. Using prefabricated-oriented fibre UHPC link slabs partially solves these issues and streamlines maintenance and replacement procedures. While there have been practical applications of oriented fibre UHPC in bridge decks [70,71], further theoretical research and practical implementation of prefabricated link slabs are needed. Most studies have concentrated on cast-in-place link slabs, whereas precast link slabs, particularly when using ECC, might offer more practical solutions [51].

A main challenge in prefabricated link slabs is selecting the proper fastening system, such as adhesive bonding and mechanical connections. Adhesives can be temperature-sensitive, posing failure risks under varying temperatures. Mechanical fasteners like dowel connectors, open-hole steel plate connectors, and bolt connectors are commonly used in prefabricated composite structures. However, studies on connecting main beams to link slabs using bolts are limited [72–75], identifying two predominant types of failure: concrete crushing and bolt shear failure. Some scholars recommended increasing concrete strength, bolt diameter, and embedment slenderness ratio to increase connector shear capacity during concrete crushing [76]. Liu et al. [77] discovered that increasing the bolt-hole size enhanced connector stiffness and load-bearing capacity. Chen et al. [76] also found that the pretension level did not affect the ultimate load-bearing capacity of bolt connectors, only influencing the initial slip between components.

No study to date has examined the sensitivity of the mechanical performance of prefabricated link slabs to fibre orientation in UHPC. Therefore, the main focus and originality of this research lie in its specific emphasis on prefabricated, rather than cast-in-situ, link slabs and the experimental characterization of the impact of fibre orientation on the bending behaviour of these slabs. Additionally, there is a lack of knowledge regarding the combined effect of UHPC, the thickness of the unbonded layer, and the bolt edge distance on their behaviour, which this research also addresses. Therefore, this study presents an extensive experimental campaign on full-scale prefabricated UHPC link slabs fastened with high-strength bolts to understand the effects of (i) material selection (RC vs. UHPC), (ii) optimization of steel fibre orientation (random vs. oriented), and (iii) different geometric features of the slab, specifically bolt edge distance and the thickness of the unbonded layer.

2. Description of the experimental tests

2.1. Experimental design

The link slab geometry tested in this paper has been inspired by that adopted in the Zhangzhou Shili Bridge [78–82], shown in Fig. 3. This bridge is a six-span, simply supported beam-like structure with extended deck slabs at the abutments. It has a span of 16 m and a width of 12.25 m. The superstructure comprises RC hollow slab beams, each measuring 0.85 m in height and 0.89 m in width. There are 11 link slabs laid transversely across the main beams. The expansion joint width between adjacent main beams at the pier is 0.08 m. According to the Chinese Code [83], the bridge is designed to bear highway class I loads.

According to the literature, the length of the link slab can be set 5% of the span lengths of the adjacent main beams [24,46] Consequently, the specimen length was determined to be 1680 mm, calculated as (5% × 2 × 16 000 mm + 80 mm), which includes 5% of the span lengths of the adjacent main beams (2 × 16 000 mm) and the expansion joint width between them (80 mm). A standard link slab thickness of 100 mm [46] was selected for the specimen. The width of the specimen was set equal to the width of each RC hollow slab beam used in the case study.

The authors tested a structural assembly comprising prefabricated link slabs on two concrete beam segments with an elastomeric debonding layer beneath. Table 1 presents the geometric and material characterization of all the tested experimental configurations. The paper focuses on the short-term mechanical response of the link slab, neglecting the mechanical characterization related to long-term behaviour under repeated load cycles, such as fatigue phenomena.

Fig. 3. View of Zhangzhou Shili Bridge.
Source: Photo taken by the author Junqing Xue.

Table 1
Geometric and material characterization of all the tested experimental configurations, where V_f is the volumetric fraction of steel fibres, d is the bolt edge distance, and h is the thickness of the unbonded area (see Fig. 4).

Test groups	Label	Test repetitions	Material	V_f [%]	d [mm]	h [mm]
Geometry	UHPC-d100-h5	3	UHPC-R	2	100	5
	UHPC-d200-h5	3	UHPC-R	2	200	5
	UHPC-d300-h5	3	UHPC-R	2	300	5
	UHPC-d400-h5	3	UHPC-R	2	400	5
	UHPC-d100-h0	3	UHPC-R	2	100	0
Material	RC (C50)	3	UHPC-R	/	100	5
	UHPC-R-Vf2	3	UHPC-R	2	100	5
	UHPC-O-Vf1	3	UHPC-O	1	100	5
	UHPC-O-Vf2	3	UHPC-O	2	100	5
	UHPC-O-Vf3	3	UHPC-O	3	100	5

Table 1 can be divided into two sections, labelled geometry and material, indicating the nature of the main variables considered. The same material was used in the first group, UHPC, with randomly oriented fibres and a volumetric fraction of 2%. The parameters changed were d, which is the distance from the row of bolts to the edge (100, 200, 300, and 400 mm), and h, the thickness of the unbonded layer consisting of a thin elastomeric layer, either 5 mm thick or absent, as in the last configuration (see Fig. 4). The selection of these two variables, d and h was based on preliminary numerical analysis.

The second group is characterized by constant geometry. The authors tested link slabs made of UHPC by varying both the fibre orientation (oriented (O-UHPC) vs. randomly oriented (R-UHPC)) and the volume of steel fibres (V_f) with the following percentages: 1%, 2%, and 3%. The geometry of the UHPC specimen was chosen according to the results of trial tests. Such configuration includes a 5 mm thick unbonded layer and a bolt edge distance of 100 mm. All the tested link slabs are 1680 mm long, 100 mm thick, and 890 mm wide; the width is based on a single hollow slab beam's transverse dimension.

Fig. 4 shows the details of the steel reinforcement of the link slab. A steel mesh layer was embedded at the midpoint of the specimen's thickness, comprising 6 longitudinal and 17 transverse HRB400 ⌀12 steel bars with spacings of 162 mm and 100 mm, respectively. Each specimen had four bolt holes at the ends for fastening to the main beams, with circular holes allowing for a 10 mm longitudinal expansion. The M27 bolts with a diameter of 27 mm and a length of 100 mm were chosen. The M27 steel bolts comply with the ASTM A490 standard [84]. They have a tensile strength of about 1040 MPa and yielding strength of 940 MPa.

The benchmark RC link slab is made of C50 strength class concrete.

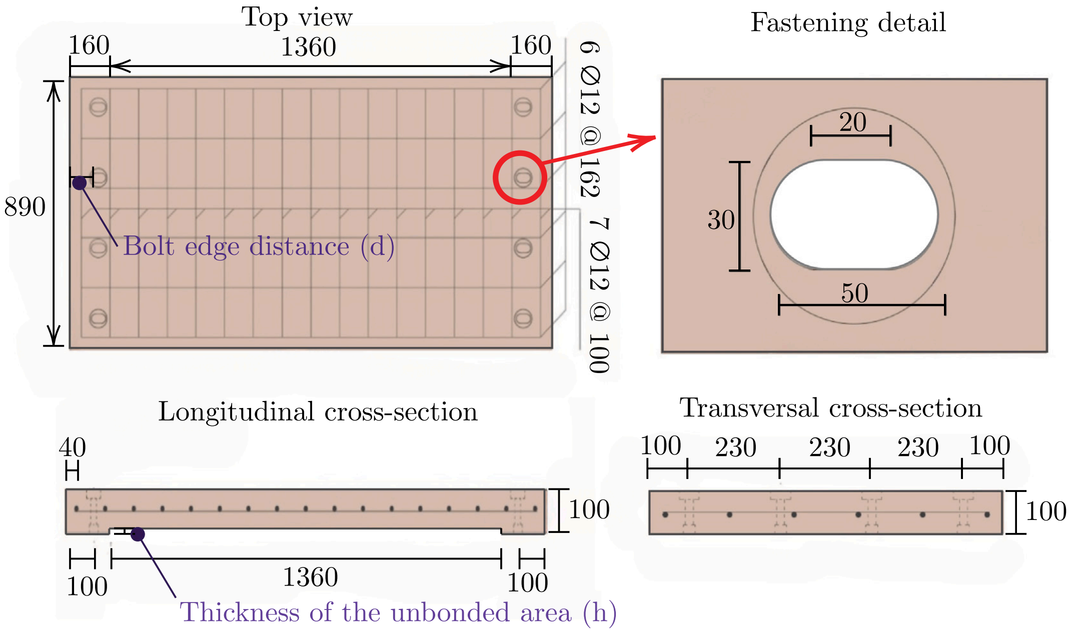

Fig. 4. Details of the reinforcement of the link slab. The units are in mm.

2.2. *Specimen preparation*

The specimen preparation consisted of two primary phases. The first phase involved fabricating the link slab. The second phase focused on assembling the complete specimen for bending tests, which included fastening the link slab to two concrete girder segments using high-strength bolts.

2.2.1. *Link slab preparation*

The steps taken to prepare for casting specimens started with the formwork fabrication. Fig. 5 shows some steps of the phases before casting the link slab. Holes, each with a diameter of 10 mm, were drilled at the predetermined positions for the bolt holes on the bottom of the formwork. Thin rod bolts were inserted through these drilled holes and the bolt-hole moulds. Rubber pads were employed as the unbonded layer. During the formwork setup, the rubber pad was placed at the base of the formwork for the prefabricated oriented steel fibre UHPC link slab. This ensured that the bottom of the prefabricated slab closely adhered to the rubber pad after casting.

Strain gauges measuring 5 mm × 3 mm were attached and wrapped in epoxy resin-coated fabric. The outermost longitudinal and transverse rebars were spot-welded to form a unified structure, ensuring the reinforcement mesh maintained its shape. Finally, the mesh was secured with wire ties.

The casting process for the link slabs varies between the use of randomly oriented and oriented steel fibre-reinforced UHPC [85]. The shape, size, volume content, distribution, and orientation of steel fibres significantly influence the mechanical properties of UHPC [68], as better discussed in the following section. Steel fibres aligned with the principal tensile stress direction provide a higher crack resistance. In contrast, those perpendicular to the principal tensile stress do not contribute and may even reduce UHPC strength [86]. The utilization rate of steel fibres randomly oriented in UHPC is only about 30% [87]. Therefore, by adjusting the orientation of fibres within the matrix, significant improvements can be achieved in the bending and tensile properties. The authors developed a specific casting device to achieve steel orientation in UHPC. While devices for fibre orientation based on the application of a magnetic field typically results in superior mechanical properties in oriented UHPC [88], the high dimensions of the link slabs make their application impractical. The casting device developed by the authors and shown in Fig. 6 includes an orientation channel and a vibrator, with a vibration frequency of 2860 counts per minute and an amplitude of 0.3 0.6 mm. The orientation channel, made of wooden panels, measures 1000 mm in length, 826 mm in width, and 73 mm in height. It consists of 11 horizontal channels, each 850 mm long, 50 mm wide, and 50 mm high, separated by partitions 23 mm thick. The device is set at a 30° incline on a support frame. Above the orientation channel, a 150 mm space is reserved for placing the fresh UHPC mix. A vibrator is strategically positioned at the midpoint on the underside of the orientation channel. The vibration aids in rapidly flowing the fresh UHPC mix downward, effectively aligning the steel fibres.

During the specimen preparation, once the UHPC flowed into the link slab, the orientation device was moved back and forth to spread a layer evenly. This process was repeated until the oriented steel fibre UHPC covered the entire link slab, involving 10 layers. Finally, the surface of the link slab was smoothed, and a film was applied to prevent cracking. After 24 h of resting, the link slab's formwork was removed, and all components were wrapped in large sheets of film for steam curing. The bottom of the film was covered with a wet geotextile to prevent steam leakage. The curing temperature was maintained at 90 ± 1 °C for 72 h. After the steam curing, normal temperature curing was conducted for 28 days before moving the specimens to the test site.

2.2.2. *Assemblage of the specimen*

After the link slab was made, the specimen preparation and assembly for the four-point bending tests involved two phases: constructing two concrete beam segments and the final assembly of the specimen, which included the girder segments, link slab, and rubber pads, all connected using high-strength bolts. The concrete beam segments were made with C50 strength grade concrete and measured 780 mm in length, 890 mm in width, and 200 mm in height. An integral part of the design, an L-shaped steel plate, was welded to the embedded reinforcement of the girder. This plate, ensuring optimal flatness, matched the girder in length and width and was 20 mm thick.

The assembly process involved several key steps: positioning the main beam on supports after installing and lubricating the rollers for smooth operation, using jacks for temporary support at the beam ends

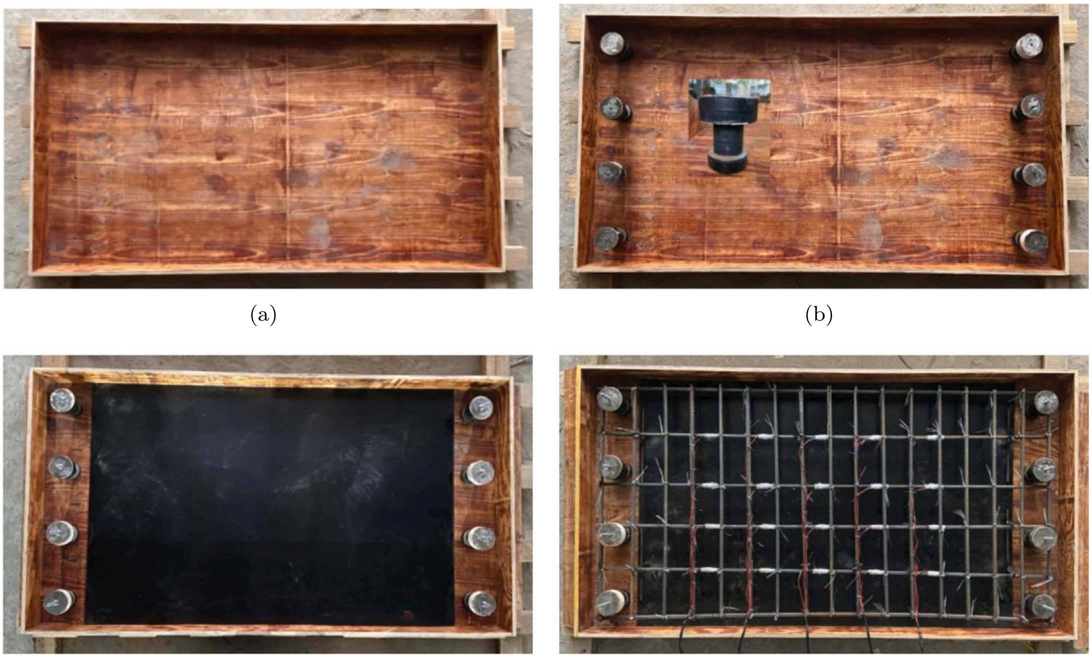

Fig. 5. Main steps in the phases before casting the link slab: (a) preparation of the formwork, (b) insertion of holes at the ends for the bolts and placement of the bolts, (c) positioning of the debonding layer, (d) insertion of the longitudinal and transverse reinforcements.

Fig. 6. Link slab preparation: (a) orientation channel for pouring oriented UHPC link slab, (b) Steam curing of the link slab.

while maintaining an 8 cm gap between the beams, marking and preparing bolt positions on the L-shaped steel plate, and performing initial tack welding of the bolts. A rubber pad was placed and levelled on the L-shaped steel plate's upper surface as debonding layer. After welding of the bolts, the link slab was fastened and secured with nuts and a sleeve. The final step involved setting up the loading supports and distribution beams for the bending tests. Selected phases of the assemblage process are depicted in Fig. 7: (a) shows the two girder segments with L-shaped steel profiles, (b) the welding of the bolts, (c) the fastening of the link slab and (d) the positioning of a steel beam for the four-point bending tests.

2.3. Experimental setup

The authors conducted four-point bending tests, as illustrated in Fig. 8. In these tests, a steel beam applied a load to the edges of the link slab while the girder segments were supported at two points. The offset between the reaction forces at the beam supports, and the forces applied at the beam edges induced the rotation of the two elements, similar to what happens in simply supported beams. Four-point bending tests were conducted to create a uniform bending moment region, which is beneficial for studying the pure bending behaviour of the link slab without the influence of shear forces. Additionally, four-point bending tests were chosen because for this kind of test it is possible to

(a) (b) (c) (d)

Fig. 7. Selected phases of the assemblage process: (a) shows the two girder segments with L-shaped steel profiles, (b) the welding of the bolts, (c) the fastening of the link slab and (d) the positioning of a steel beam for the four-point bending tests.

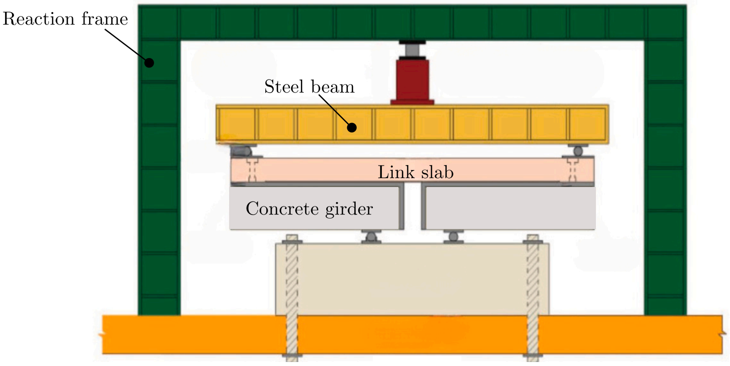

Fig. 8. Sketch of the four-point bending tests.

reliably predict the point and mode of failure, thus obtaining a more controlled experimental failure.

The rotations to be applied by the universal testing machine are based on the relevant standard codes. Specifically, the rotation angles under Service (SLS) and Ultimate Limit States (ULS) are calculated according to JTG 3362-2018 [89] using Eq. (1).

$$\theta = \frac{\Delta \times 3}{L_{\mathrm{sp}}} \tag{1}$$

These calculations take into account the maximum allowable long-term deflection (Δ) and the span length (L_{sp} = 16 m in the case study). According to JTG 3362-2018 [89], Δ should not exceed $\frac{1}{600}$ of L_{sp}. Therefore, the rotation angle (θ) specified by JTG 3362-2018 is fixed and equals 0.005.

A preliminary displacement of 0.4 mm was applied to eliminate gaps between components, ensuring the operational accuracy of the measuring devices. Loading was conducted in stages of 0.2 mm, with adjustments made when approaching specific displacement thresholds. The experiment involved detailed observation and measurement of crack formation and progression. Displacement continued until the specimen reached peak load, followed by displacement-controlled loading until failure.

A total of 20 concrete strain gauges were arranged on the middle section of the upper surface of the specimen (see Fig. 9). These

Fig. 9. (a) Installation of the strain gauges on the steel rebars, (b) experimental setup with all installed transducers.

Table 2
Main chemical composition of the cement in percentage volume (%).

SiO_2	Al_2O_3	CaO	Fe_2O_3	SO_3	MgO	f-CaO	Na	K	Alkali content
21.69	4.38	62.55	3.34	2.893	2.05	0.57	0.13	0.35	0.36

Table 3
Main chemical composition of silica fume in volume percentage (%).

CaO	SiO_2	Al_2O_3	Fe_2O_3	MgO	Na_2O	K_2O	SO_3	Pozzolanic activity index
0.63	87.67	0.28	0.60	3.41	1.30	4.12	0.84	108.6

gauges were spaced longitudinally at 200 mm intervals and laterally at 162 mm intervals. The placement of the concrete strain gauges corresponded to that of the steel strain gauges. Two additional concrete strain gauges were positioned around the middle two bolt holes on each side of the specimen, with a directional spacing of 230 mm. Additionally, five concrete strain gauges were installed at the mid-span position on the side surface of the specimen. These gauges were located at distances of 90 mm, 70 mm, 50 mm, 30 mm, and 10 mm from the bottom of the specimen, respectively, as shown in Fig. 9. The concrete strain gauges used in this study were from the Gold Foil series of resistance strain gauges provided by Chengdu Electric Measurement and Sensing Co., Ltd., with each gauge measuring 100 mm × 3 mm.

3. Material characterization

This section is dedicated to a preliminary characterization of the material properties used to make the link slab specimens.

3.1. Mix design and chemical-physical properties of UHPC components

The materials used to make UHPC include cement, silica fume, quartz sand, polycarboxylate superplasticizer, water, and steel fibres. The cement used in an Ordinary Portland Cement P.O 42.5, with a specific surface area of 371 m^2/kg. The chemical composition content is shown in Table 2.

The silica fume has a SiO_2 content greater than 90% and a particle size of 0.1–1 μm. Its mass density is 2.25 g/cm^3. The main chemical composition is shown in Table 3.

The superplasticizer is a CX-8 polycarboxylate. It has a water reduction rate of over 25%, with main performance indicators shown in Table 4.

The characteristics of the steel fibres are shown in Table 5. The chosen volume contents of steel fibres are 1%, 2%, and 3%. The composition of UHPFRC, shown in Table 6, is used as per Refs. [90–92]. The masses of the steel fibre per m^3 are 78, 156, and 234 kg, corresponding to 1, 2, and 3% fibre volume fractions, respectively. The masses of the other constituents remain the same. The water/binder ratio is 0.18.

The following steps were implemented to mitigate the clustering of the steel fibres during the mixing process. First, cement, quartz sand, and silica fume were poured into the mixer and mixed for 5 min. To prevent the clustering of steel fibres, they were gradually added during the mixing process and stirred for 5 min after the complete addition. The pre-measured superplasticizer was slowly introduced into water and mixed to form a solution. Two-thirds of this solution was added to the mixture and then mixed until it achieved a dough-like consistency. Subsequently, the remaining solution was added and mixed for another five minutes.

For specimens with randomly oriented steel fibres in UHPC, the freshly mixed UHPC was placed into moulds using a trowel. Conversely, the oriented channel method was employed for specimens with oriented steel fibres, as shown in Fig. 6. The steel fibres gradually aligned as the freshly mixed UHPC flowed through the channel. The application of vibration beneath the inclined channel enhanced the flow of UHPC. UHPC was gradually poured from the top end of the oriented channel and swiftly flowed under the influence of vibration. The mould was shifted in alignment with the orientation direction of the steel fibres, casting layer by layer until the mould was filled. This method of preparing oriented steel fibre UHPC adhered to the "Reactive Powder Concrete" standard (GB/T 31387-2015) [93].

Post-casting, all specimens were covered and left outside for 24 h before demolding. Once moulded, the specimens were subjected to steam curing in a chamber maintained at 90 °C ± 1 °C for 72 h. The specimens were covered with a wet cloth underneath the film to prevent steam leakage and ensure effective curing. The specimens underwent room-temperature curing following steam curing, and their material properties were evaluated on the 28th day.

3.2. Computer-Tomography Scanning of UHPC specimens

X-ray CT scanning was employed to evaluate the orientation effect of steel fibres in UHPC, followed by a three-dimensional reconstruction of steel fibres from the scanned images. Specimens from the four-point bending test were selected for this purpose. The optimal sample size for maximum efficiency and quality in the scanning equipment is 20 mm. Therefore, using a rock-cutting machine, the specimens were cut 1.5 times the fibre length (20 mm) from the fracture surface, ensuring the steel fibres remained intact. To minimize the impact of mould sidewall effects on the scan, 30 mm was trimmed from the edges of the specimen section, leaving a central portion measuring 40 mm × 40 mm. This portion was then longitudinally cut to a length of 30 mm. Subsequently, the sample was polished into a cylinder with a diameter of 20 mm and a height of 30 mm, as illustrated in Fig. 10.

The CT scanning equipment used in this experiment was the Zeiss Xradia 510 Versa 3D X-ray microscope, as shown in Fig. 11(a). The sample was glued to the sample stage using AB glue and placed in the scanning chamber, adjusting the height of the sample stage to the appropriate position, as illustrated in Fig. 11(b). Scanning was performed at a voxel resolution of 40.2 μm, with a 4X objective lens magnification.

Table 4
Technical indicators of CX-8 polycarboxylate superplasticizer.

Appearance	Water reduction rate	Density (g/mm)	pH value	Solid content (%)	Chloride ion content	Total alkali
Pale Yellow	≥25%	1.08 ± 0.02	7.0 ± 1	30 ± 1	≤0.2%	≤10.0%

Table 5
Main parameters of steel fibre where the density and strength are expressed in kg/m^3 and MPa, respectively.

Type	Shape	Length/diameter (mm)	Aspect ratio	Dens.	Young's modulus	Tens. strength
Wire-type	Straight round	13/0.2	65	7850	200	≥2000

Table 6
UHPC mix design per cubic meter (kg/m^3).

Steel fibre	Cement	Silica fume	Quartz sand - Mesh [mm]				Superplasticizer	Water
			0.85–2	0.425–0.85	0.212–0.425 Mesh	0.0374		
78 156 234	859.5	258	452.5	352	120.5	80.5	21.5	179

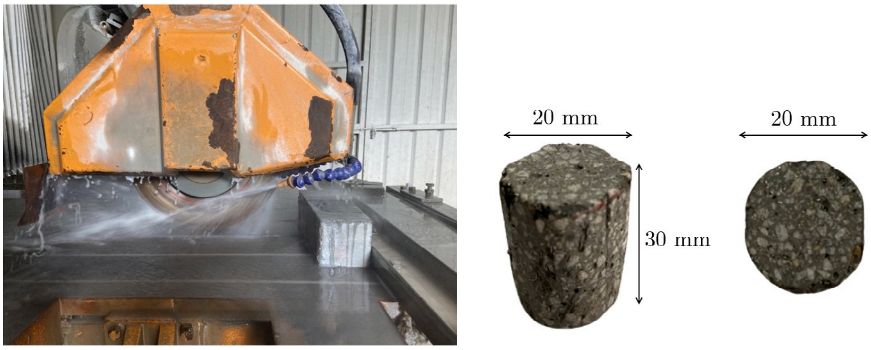

(a) (b)

Fig. 10. (a) Sample cutting (b) Material sample used for CT scan.

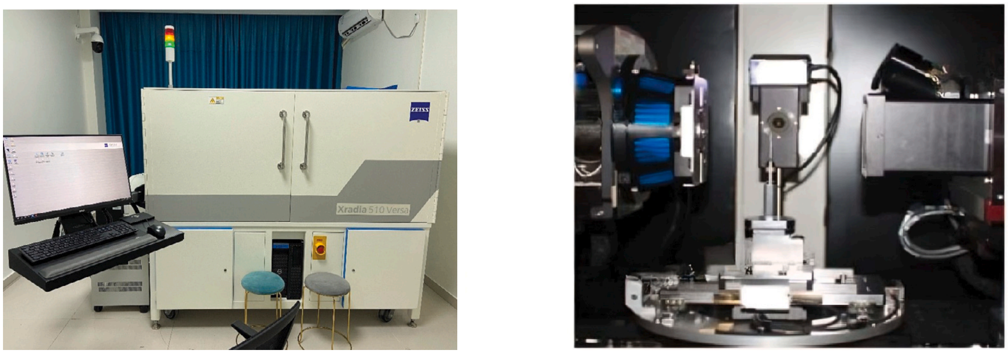

(a) (b)

Fig. 11. CT scanning equipment: (a) Zeiss Xradia 510 X-ray microscope (b) Inside view of the microscope.

Fig. 12 shows the triaxial 2D slice images of a UHPC sample with 2% V_f and oriented steel fibres, with the y-direction representing the orientation direction of the steel fibres and the x and z-directions perpendicular to y. There were 779 slices in the y-direction and 812 slices each in the x and z directions. One slice from each direction was chosen for analysis. In the slice images, the cross-sections of the steel fibres appeared white with high brightness, the matrix was grey, and the voids were black. In Fig. 12, the cross-sectional images of the steel fibres were nearly circular, indicating that the fibres were almost perpendicular to the slice direction.

Due to the density and brightness difference between steel fibres and matrix, adjusting the grayscale threshold allowed the visual separation of the steel fibres from the matrix, resulting in the binary image shown in Fig. 12 where the contours of the steel fibre cross-sections are clearly identifiable. By measuring the long axis (l) and short axis (d) of the steel fibres in the figures, the orientation angle (θ) of the steel fibres can be calculated using Eq. (2), and the orientation coefficient (η_θ) using Eq. (3).

$$\theta = \arccos\left(\frac{d}{l}\right) \tag{2}$$

$$\eta_\theta = \int_{\theta_{\min}}^{\theta_{\max}} p(\theta)\cos^2(\theta)d\theta \tag{3}$$

In Eq. (3), $p(\theta)$ represents the probability density function of the fibre orientation angle. The terms $\theta_{\min}$ and $\theta_{\max}$ denote the minimum

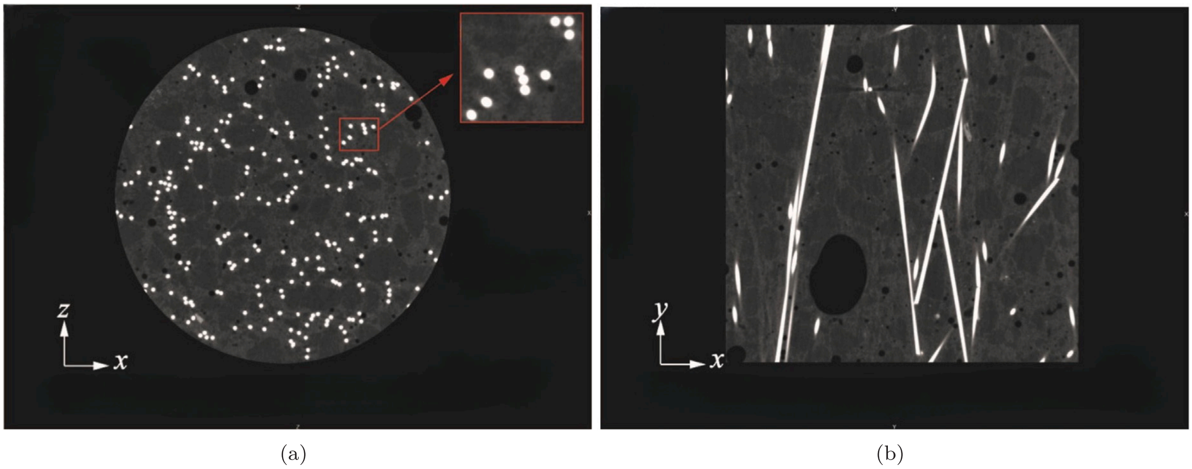

(a) (b)

Fig. 12. Two-dimensional slice images of the sample scan: (a) $x - z$ slice (b) $x - y$ slice.

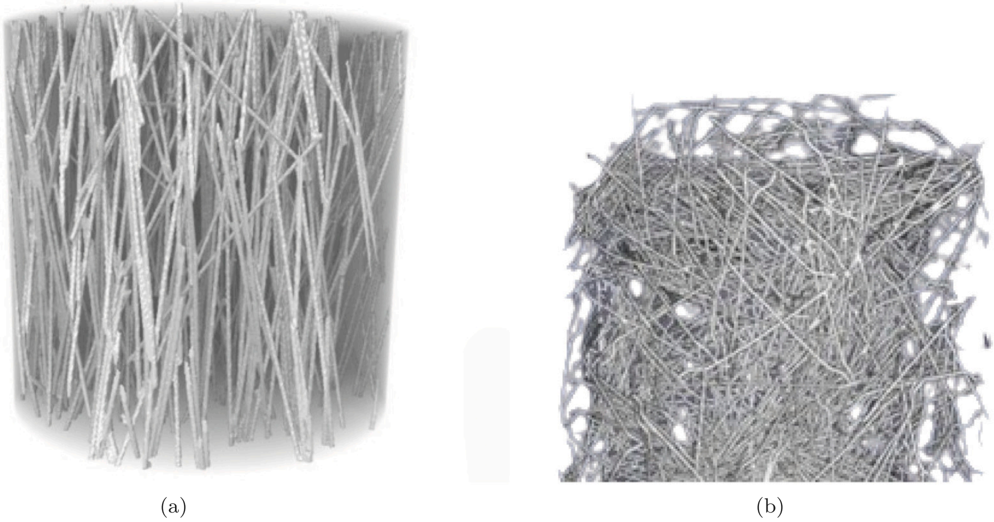

(a) (b)

Fig. 13. Three-dimensional reconstruction images of steel fibres (a) UHPC with 2% V_f and oriented fibres (b) UHPC with 2% V_f and random fibres [95].

and maximum angle orientations, respectively. The range of θ is from 0° to 90°, while the range of η_θ is from 0 to 1. A θ of 0° indicates that the steel fibres are aligned with the set direction (the corresponding η_θ is 1). In contrast, a θ of 90° indicates that the steel fibres are perpendicular to the set direction (the corresponding η_θ is 0). An η_θ value closer to 1 signifies a more effective fibre orientation. Each $x - z$ slice was analysed in the Dragonfly software [94], to reconstruct the spatial distribution of steel fibres.

Fig. 13 presents the three-dimensional reconstructed images of two samples, one with oriented fibres and the other with randomly oriented fibres. Most steel fibres in the oriented sample are aligned along the y-direction. The orientation coefficients in Eq. (3) for the oriented samples were about $\eta_\theta = 0.89$, whereas they were nearly zero for the randomly oriented fibres, revealing a chaotic and highly random orientation.

3.3. Mechanical characterization of UHPC

The mechanical characterization of the UHPC specimens is based on the tests shown in Fig. 14: compression, tensile and bending tests and separate compression tests for assessing Young's modulus. The specimens comprise UHPC with randomly oriented and oriented steel fibres, with the volume fraction of steel fibres (V_f) equal to 1%, 2%, and 3%. Each material test comprises three cubic specimens for compression tests (dimensions: 100 mm × 100 mm × 100 mm), six prismatic specimens for Young's modulus assessment (dimensions: 100 mm × 100 mm × 300 mm), three dog-bone shaped specimens with a smaller cross-section (50 mm × 50 mm) for tensile tests and three specimens for four-point bending tests (dimensions: 100 mm × 100 mm × 400 mm).

The compression tests were carried out as per the "Reactive Powder Concrete" standard (GB/T 31387-2015) [93]. A 2000 kN electro-hydraulic servo press was used with a loading rate of 1.2 MPa/s. The tests assessing Young's moduli also followed the same standard [93]. In contrast, the tensile tests were carried out according to the "fibre Reinforced Concrete Test Method Standard" (CECS13:2009) [96]. The load was applied using a 300 kN universal testing machine at a 0.2 mm/min rate. Lastly, the bending tests were carried out also following the standard [96] and the relevant provisions of the American ASTM C1609/C1609M-19a [97]. Table 7 shows the results of the experimental tests on the UHPC specimens in terms of mean and coefficient of variation (CoV).

Fig. 15 displays the average stress–strain and stress–displacement curves for the tensile and bending tests, respectively. It can be noted that the relative variation in compressive strength between specimens with randomly oriented and oriented fibres with 2% fibre is about 7%, while the effect of fibre orientation has smaller effects on Young's modulus and Poisson's ratio.

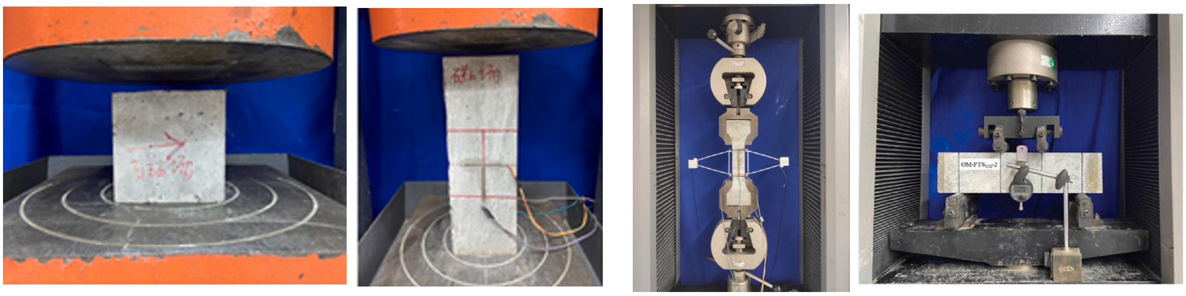
(a) (b) (c) (d)

Fig. 14. View of the experimental tests carried out on the UHPC specimens: (a) compression test; (b) Young's modulus estimation; (c) tensile test; (d) bending test.

Table 7
Mean and coefficient of variation (CoV) of the test results on the UHPC specimens with and without fibre orientation and a 2% steel fibre content.

Parameter	Symbol	Unit	R-UHPC (2%)		O-UHPC (1%)		O-UHPC (2%)		O-UHPC (3%)	
			Mean	CoV	Mean	CoV	Mean	CoV	Mean	CoV
Compressive strength	f_c	[MPa]	163.12	0.011	166.21	0.189	175.32	0.189	169.60	0.018
Young's modulus	E	[GPa]	45.30	0.005	46.10	0.006	46.60	0.006	48.10	0.006
Poisson ratio	ν	[–]	0.21	0.006	0.21	0.005	0.21	0.005	0.21	0.005
Tensile strength	f_t	[MPa]	6.13	0.014	6.93	0.129	9.57	0.129	13.24	0.013
Bending strength	f_b	[MPa]	18.90	0.019	25.10	0.025	28.58	0.256	34.20	0.256

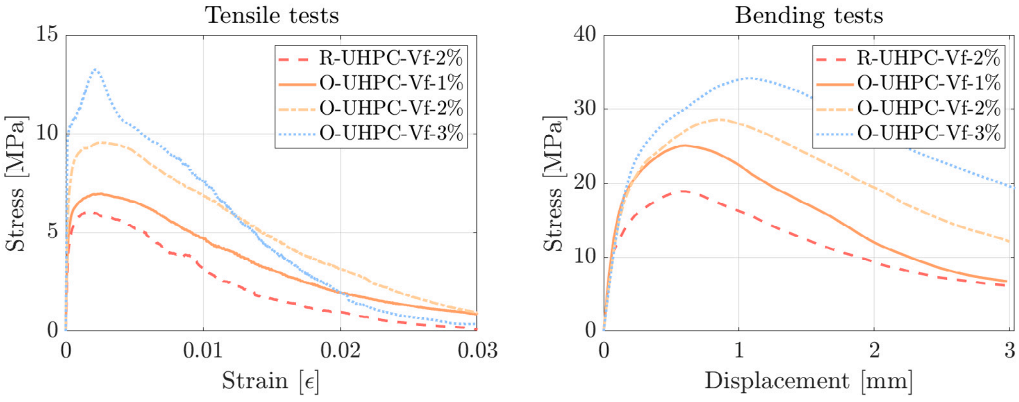

(a) (b)

Fig. 15. Average (a) stress–strain and (b) stress–displacement curves for the tensile and bending tests, respectively.

The improvement related to fibre orientation can be primarily observed from the variation in tensile and flexural strength, with an average relative improvement of 56% and 51% in the mentioned specimens, respectively. This confirms that fibre orientation maximizes their function and is highly beneficial. Regarding the fibre volume percentage in specimens with oriented fibres, a clear improvement of 5% in compressive strength and 38% and 14% in tensile and flexural strength, respectively, can be seen when increasing from 1% to 2% fibre. However, increasing from 2% to 3% did not show any improvement in compressive strength and Young's modulus. Still, there was a further improvement in tensile and flexural strength of 38% and 20%, respectively, when increasing from 2% to 3%, with an almost linear increment relative to the volumetric variation of fibres.

Regarding the stress–strain curves for the tensile and bending tests, all specimens displayed similar trends, demonstrating strain-hardening characteristics despite different fibre orientations. Each specimen's response can be categorized into the elastic, strain-hardening, and stress-softening stages. Initially, no cracks appeared on the specimen surfaces in the linear elastic stage. However, as the load increased, stress concentration at material weak points led to micro-crack formation. Further loading prompted the continuous development of these micro-cracks. The steel fibres bridging the cracks transferred stress to the uncracked matrix, forming multiple cracks. The specimens with oriented steel fibre UHPC displayed higher fibres performing a bridging role than those with random orientation. This difference delayed crack development and enhanced crack resistance. With continued load application, macroscopic cracks formed from merging several micro-cracks, culminating in peak load. Subsequently, the main crack widened, forming a macroscopic failure surface. Interestingly, the load did not drop rapidly at this stage due to the support provided by the adhesion and sliding of steel fibres within the matrix. Fig. 16 illustrates the ultimate state of the UHPC with randomly oriented and aligned fibres. In specimens with randomly oriented fibres, the steel fibres are distributed chaotically but uniformly in the specimens. Conversely, most steel fibres are aligned in the same direction in the specimens with oriented fibres.

3.4. Normal concrete and steel

The RC used for casting the link slab and the concrete girder segments is a C50 commercial concrete, see Fig. 17. Three cubic test blocks (150 mm × 150 mm × 150 mm) were prepared to estimate the compressive strength, and six prismatic test blocks (150 mm × 150 mm × 300 mm) to evaluate Young's modulus. Additionally, three dog-bone

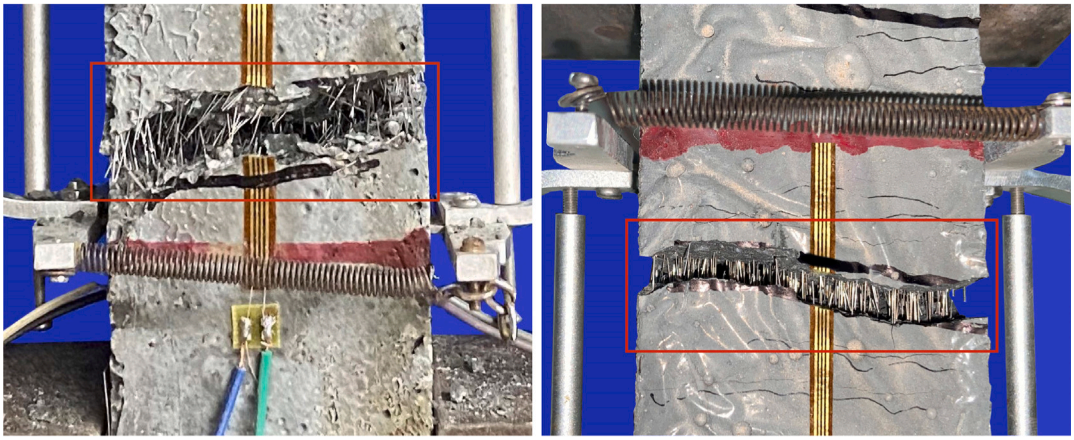
(a) (b)

Fig. 16. Fracture surface after tensile tests on the UHPC specimens with (a) randomly oriented and (b) oriented fibres.

(a) (b) (c)

Fig. 17. View of the experimental tests carried out on the RC and rebar specimens: (a) compression test on the RC specimens; (b) Young's modulus estimation on the RC specimens; (c) tensile test on the rebar specimens;.

Table 8
Mean and coefficient of variation (CoV) of the test results on the C50 concrete specimens.

Parameter	Symbol	Unit	Concrete (C50)	
			Mean	CoV
Compressive strength	f_c	[MPa]	52.10	0.025
Young's modulus	E	[GPa]	40.6	0.005
Poisson ratio	ν	[–]	0.21	0.006
Tensile strength	f_t	[MPa]	1.13	0.080
Bending strength	f_b	[MPa]	12.50	0.030

Table 9
Mean and coefficient of variation (CoV) of the test results on the reinforcing steel bars.

Yielding strength [MPa]		Ultimate strength [MPa]		Young's modulus [GPa]	
Mean	CoV	Mean	CoV	Mean	CoV
418.00	0.011	605.00	0.017	201.00	0.009

specimens, identical in dimensions to those used for UHPC, were cast to assess the tensile strength. The material property testing followed the "Test Method Standard for Mechanical Properties of Ordinary Concrete" (GB/T50081-2019) [98].

Table 8 displays the mean and CoV of the test results on the C50 concrete specimens. Compared to UHPC, a significant reduction in tensile strength of about one-tenth is observed, while the compressive strength is in line with that of the concrete class. Consistent with "Tensile Testing of Metallic Materials Part 1" (GB/T 228.1-2010) [99], tests were performed to estimate the material properties of the steel rebars, see Fig. 17. The yield strength, ultimate strength, and Young's modulus are detailed in Table 9.

4. Experimental results on the link slabs

4.1. Effect of the link slab geometry: bolt edge distance (d) and unbonded layer thickness (h)

Fig. 18 shows the mechanical response of the link slab as the chosen geometric parameters vary, including the distance to the edge of the bolts d and the height of the unbonded layer h, for a total of five test configurations, using UHPC material with 2% V_f. Specifically, Fig. 18 displays average characteristic curves of the tested link slabs showing the applied force vs. midspan deflection (Fig. 18(a)), the applied force vs. upper side concrete deformation (Fig. 18(c)), and the applied force vs. lower side concrete deformation (Fig. 18(d)). Additionally, Fig. 18(b) shows the girder rotation vs. crack width. The behaviour of the curves is quite similar among the five configurations, with four main stages.

In Stage I, the elastic stage, no visible cracks are present on the surface of the specimen, and the force–displacement curve is approximately linear. UHPC structures, at this stage, show minimal impact on durability even when the maximum crack width is less than

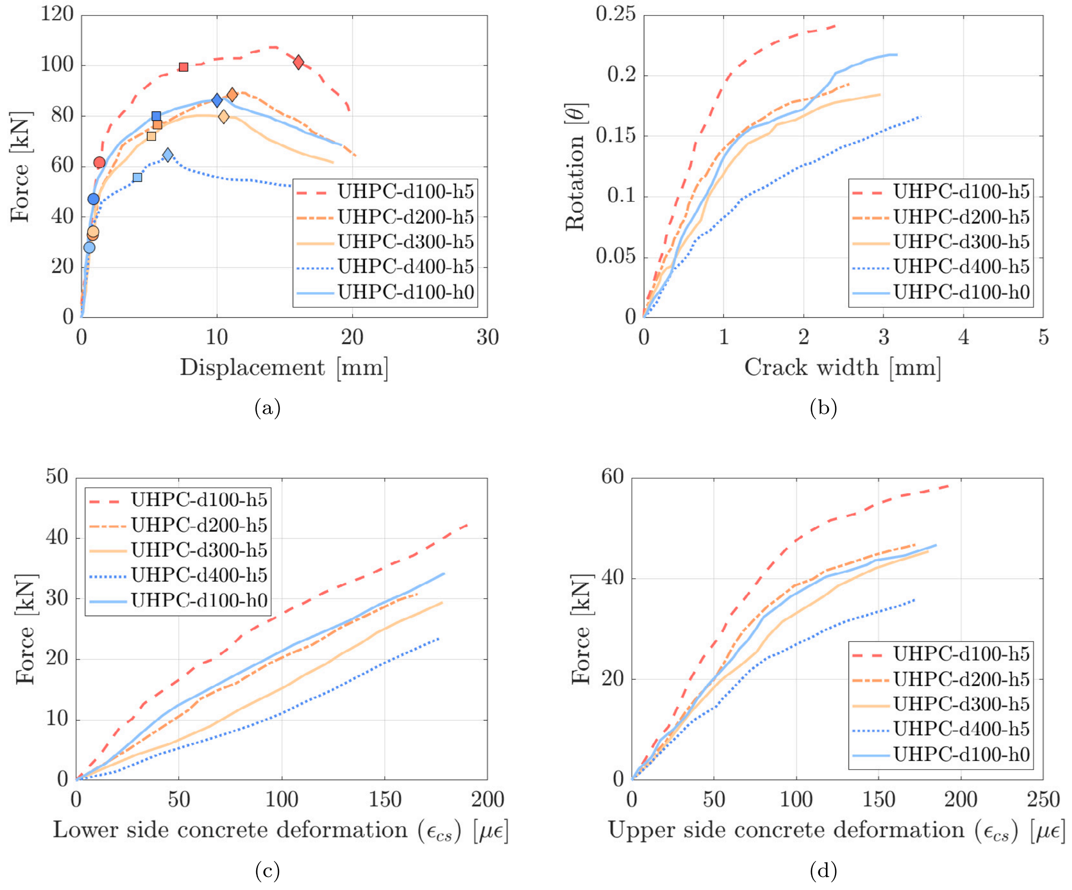

Fig. 18. Average characteristic curves of the tested link slabs showing the applied force vs. (a) midspan deflection, (c) upper side concrete deformation and (d) lower side concrete deformation. (b) Girder rotation vs. crack width. The markers in (a) identify the beginning of Stage II (circle), Stage III (square) and Stage IV (diamond).

0.05 mm [100,101]. The onset of visible microcracks characterizes stage II. When the first crack with a maximum crack width larger than 0.05 mm, defined as the initial crack, was observed by using the Digital Concrete Crack Width Gauge Meter Tester, a sudden change in bending stiffness occurred, corresponding to the inflexion point on the force–displacement curve (d_c). The directional orientation of steel fibres plays a crucial role in bridging these microcracks, ensuring that stiffness does not decrease significantly. The steel fibres distribute the tensile stress to the uncracked surrounding matrix, forming new cracks in weaker zones. This is macroscopically observed as an increase in the number of cracks, a reduction in their spacing, and an expansion of the cracked area.

As the force increases, the bond between the steel fibres and the matrix begins to weaken, reducing the inhibitory effect on crack propagation. The longitudinal tensile steel strain gradually increases, eventually leading to yield, corresponding to the yield displacement (d_y). Stage III is the yield stage, wherein a significant crack is observed. This results in a marked reduction in stiffness, and the force–displacement curve is almost constant. The specimen reaches its ultimate force (F_u), with the corresponding displacement defined as the ultimate displacement (d_u). Stage IV, the final stage, is characterized by the failure of the bonding effect between the steel fibre and the matrix at the main crack, leading to continuous pull-out of the steel fibres. The load-bearing capacity loss can be observed when the force reaches 85% of F_u.

In all the curves–whether in terms of load–displacement, rotation, crack amplitude, or applied force versus concrete side deformation–it is evident that the force and rotation increase with the increase in the edge distance of the bolts. Additionally, the farther apart the bolts are, the smaller the lever arm that can develop between them and the centroid of the link slab. It is also noted that as d increases from 200 to 400 mm, there is a substantial change in maximum force and a reduction in stiffness. It can be inferred that the configuration with the best mechanical performance is the one with $d = 100$ mm. Regarding the height of the unbonded layer, a considerable effect is observed, with a reduction of maximum force, ductility, and stiffness, when comparing $h = 5$ to $h = 0$, with a constant $d = 100$ mm. This occurs because the absence of an unbonded layer does not allow for a uniform distribution of tensile stresses confined to the central area, thereby reducing the potential to fully exploit the properties of UHPC.

Table 10
Characteristic parameters of the force–displacement curves: d_c is the first-cracking displacement, d_y the yielding displacement and d_u the ultimate displacement, F_u the maximum force and K_0 the slab initial stiffness which is determined as the tangent stiffness at the curve's origin.

Test label	d_c [mm]	d_y [mm]	d_u [mm]	F_u [kN]	K_0 [kN/mm]
UHPC-d100-h5	1.3	7.2	16	107.2	36.8
UHPC-d200-h5	0.9	5.4	11.3	89.8	33.8
UHPC-d300-h5	0.82	5	10.6	80.2	32.2
UHPC-d400-h5	0.6	4.1	6.3	64.6	23.5
UHPC-d100-h0	0.93	5.8	10.1	87.4	30.4

Table 10 allows quantification of the differences exhibited in the mechanical response of the 5 link slab configurations. Particularly, a reduction of approximately 30% in displacement associated with the first cracking and yielding can be noted when moving from $d = 100$ to $d = 200$. This includes a 16% reduction in the maximum force and an 8% reduction in stiffness. Hence, it is evident that the effects on stiffness are modest, with a greater impact on ductility and ultimate bending strength . Moving from $d = 200$ to $d = 300$, the decreases in

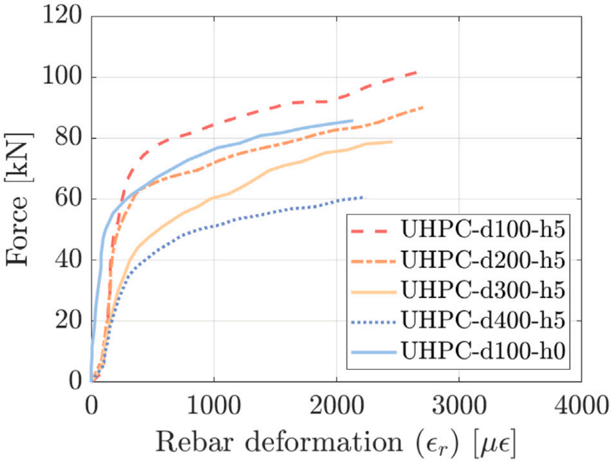

Fig. 19. Average characteristic curves of the tested link slabs showing the applied force vs. the steel rebar deformation.

the first crack, yielding, and ultimate displacements are less than 10%, while the ultimate bending strength reduces by 10%. However, moving from $d = 300$ to $d = 400$, the effects are quite significant, with a reduced ultimate displacements of about 20%.

Comparing samples with $d = 100$ but different values of h, 5 and 0 mm, a difference is observed in all parameters: the ultimate displacements decreases by 18%, while the ultimate and yielding displacements decrease by 36% and 20%, respectively. This demonstrates that even a small 5 mm gap significantly alters the link slab's mechanical behaviour.

Regarding deformation on the concrete side, positive tensile deformations are observed on both the top and bottom sides. However, the deformation on the bottom side is less, with an almost linearly elastic response up to failure. In contrast, on the top side, which deforms more, there is evidence of plasticization both in the top rebar, as shown in Fig. 19, and in the fibres embedded in the cementitious matrix.

Table 11
Main characteristics of the surface cracks on the tested specimens.

Specimen number	Crack distribution range (cm)	Number of cracks	Average crack spacing (mm)	Average crack width (mm)
UHPC-d100-h5	−30 30	65	9.2	0.19
UHPC-d200-h5	−30 30	48	12.5	0.28
UHPC-d300-h5	−30 20	36	13.8	0.32
UHPC-d400-h5	−20 20	25	16.0	0.37
UHPC-d100-h0	−20 20	30	13.3	0.36

The crack patterns of link slabs with varying bolt edge distances (d) are shown in Fig. 20. They display a principal crack and several minor cracks. As the edge distance increases, the number of minor cracks decreases, and their width increases, as quantified in Table 11, which details the number of cracks, spacing, and average width. Also the development pattern of the maximum crack width on the top surface of specimens varies with bolt edge distance. A decrease in edge distance leads to a closer longitudinal distance between bolt rows, a reduction in the effective length of the connection plate, and a decrease in the plate area subjected to negative bending moments, concentrating stress towards the centre. The bolt edge distance do not affect the crack pattern at failure, characterized by a main crack on the top surface within the range of −10 to 10 cm.

According to highway bridge regulations, the maximum width of concrete cracks under normal use should not exceed 0.2 mm. For UHPC-d100-h5, the maximum crack width on the top surface stays below 0.2 mm. However, for UHPC configurations with higher d values, the maximum crack width exceeds 0.2 mm at different limit states. UHPC-d100-h5 meets the criteria of maximum crack width being less than 0.2 mm under SLS, ULS, AASHTO standards, and highway bridge regulations.

As the bolt edge distance increases, the number of cracks and the crack distribution area on the surface of the bending specimens decrease while the average crack width and average crack spacing increase. Specifically, the number of cracks for specimen UHPC-d100-h5 (65 cracks) is 1.35, 1.8, and 2.6 times that of specimens UHPC-d200-h5,

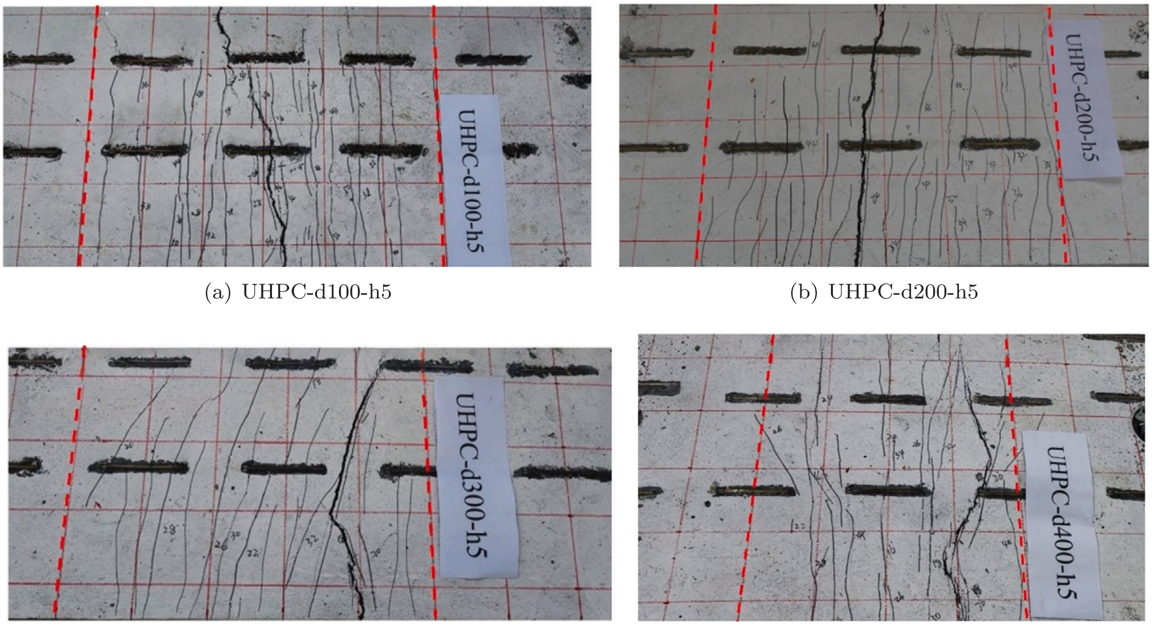

(a) UHPC-d100-h5

(b) UHPC-d200-h5

(c) UHPC-d300-h5

(d) UHPC-d400-h5

Fig. 20. Crack patterns of the link slabs with different values of the bolt end distance (d) and the thickness of the unbonded layer (h).

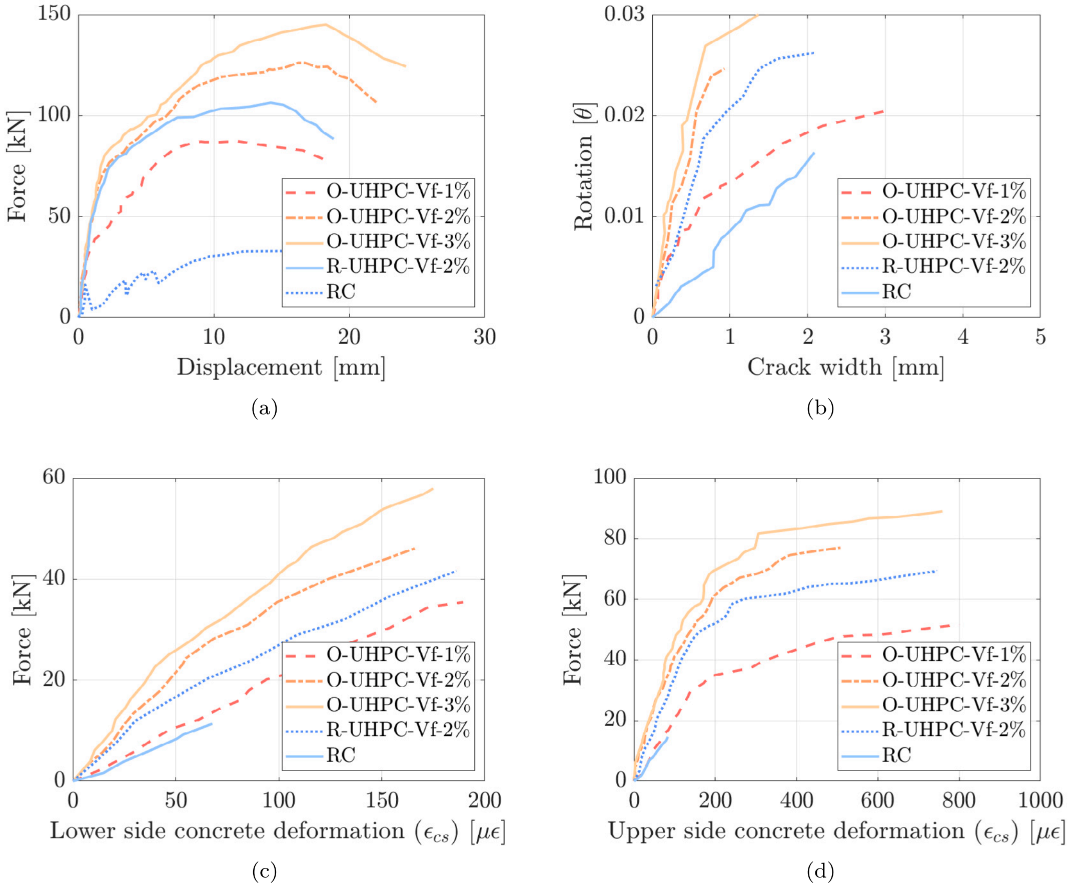

(a)

(b)

(c)

(d)

Fig. 21. Average characteristic curves of the tested link slabs showing the applied force vs. (a) midspan deflection, (c) upper side concrete deformation and (d) lower side concrete deformation. (b) Girder rotation vs. crack width.

UHPC-d300-h5, and UHPC-d400-h5 (48, 36, and 25 cracks respectively). The average crack spacing for UHPC-d100-h5 (9.2 mm) is 73.6%, 66.7%, and 57.5% of that for UHPC-d200-h5, UHPC-d300-h5, and UHPC-d400-h5 (12.5 mm, 13.8 mm, and 16.0 mm respectively). The average crack width for UHPC-d100-h5 (0.19 mm) is 67.9%, 59.4%, and 51.4% of that for UHPC-d200-h5, UHPC-d300-h5, and UHPC-d400-h5 (0.28 mm, 0.32 mm, and 0.37 mm respectively).

4.2. Effect of randomly oriented and oriented fibres in UHPC

Fig. 21(a) presents the average force–displacement curves for the five tested configurations. This allows for an analysis of various influences: RC versus R-UHPC, followed by comparing fibre orientations between R-UHPC and O-UHPC. Furthermore, the effects of the volumetric fraction of steel fibres are evaluated among the link slabs with oriented fibres.

A qualitative difference is observed between the response of RC link slabs and those in UHPC. While the RC specimens exhibit an irregular behaviour, characterized by a peak followed by an instantaneous drop in resistance and subsequent hardening, the UHPC link slabs show a more monotonous growth. Similarly to the previous case, four distinct phases can be identified in UHPC slabs: elastic, initial cracking until a sort of plasticization with hardening, and softening.

The rotational behaviour as a function of the crack opening, shown in Fig. 21(b), is almost linear for RC. An interesting phenomenon is observed where greater ductility, albeit with reduced stiffness, is achieved with lower fibre content. Conversely, with a higher volumetric fraction of fibres, there is a noticeable increase in stiffness accompanied by reduced ductility. A quantitative discussion based on the estimates reported in Table 12.

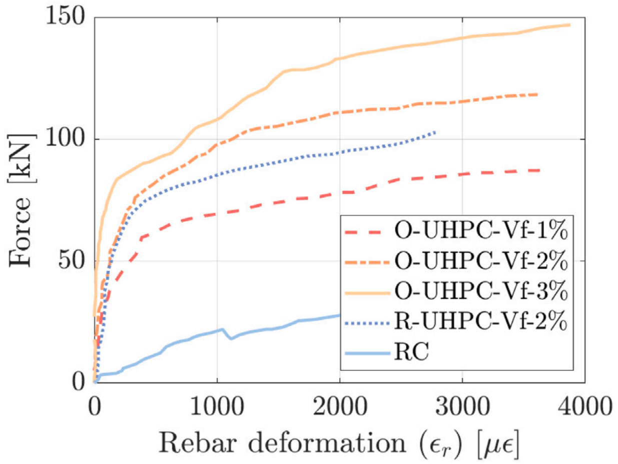

Fig. 22. Average characteristic curves of the tested link slabs showing the applied force vs. the steel rebar deformation.

Regarding the average behaviour of concrete lower side deformations, it is observed in the upper part of Fig. 21(c) that there is a nearly linear trend for all materials, with differences only in stiffness. Stiffness increases with the volumetric fraction of fibres and their orientation, and ultimate deformation is nearly one-third in RC and substantially identical for all UHPC at approximately 180–200 με.

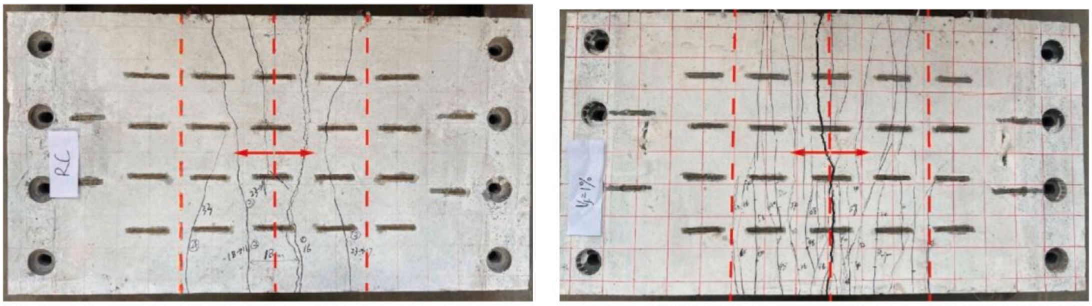

(a) RC

(b) O-UHPC-V_f-1%

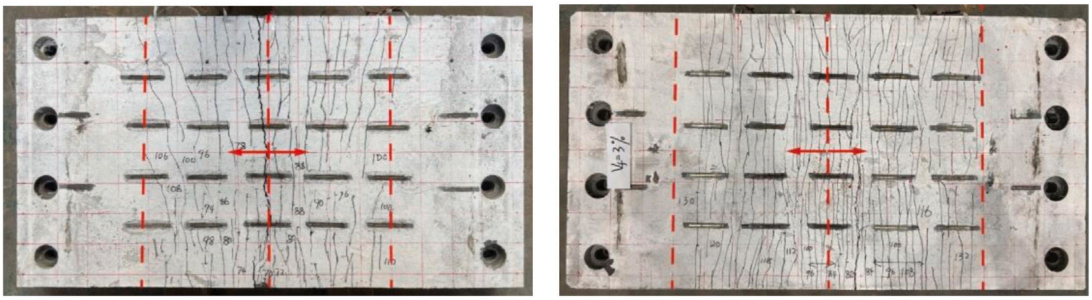

(c) O-UHPC-V_f-2%

(d) O-UHPC-V_f-3%

Fig. 23. Crack patterns of the link slabs with RC, randomly oriented (R-UHPC) and oriented (O-UHPC) UHPC and three volumetric fractions of the steel fibres.

On the other hand, the deformation on the upperside of the link slab exhibits a distinctly different pattern, as shown in Fig. 21(d): elastoplastic for UHPC and linearly elastic for RC. This difference can be easily explained by considering that the upper part of the slab is under tension and reaches the plasticity of the fibres and reinforcement steel. However, the lower part deformed less and utilizes less plasticity sources.

Fig. 22 shows the applied force as a function of the average deformation of the reinforcing bar in the tensile zone. The observed elastoplastic behaviour confirms previous findings, indicating that the reinforcements reach their plastic strength on the upper side of the slab.

The qualitative differences between the mechanical behaviours of the link slabs can also be observed in Fig. 23. In the case of RC, the cracks are fewer but wider. For UHPC with oriented fibres, the number of cracks and their width change as expected as the fibre content increases.

Table 12 presents the values of mid-span displacement associated with the initial cracking (d_c), yielding (d_y) and ultimate stages (d_u), as well as the ultimate force and the secant stiffness between 0 and the first cracking stage.

The difference in performance between UHPC and RC in applications like link slabs is rooted in their distinct material properties. While UHPC is known for its high toughness, this characteristic does not necessarily equate to the ability to endure large-scale deformations. Instead, UHPC's toughness reflects its capacity to absorb significant energy before failure.

The RC slab also has lower stiffness, with a relative decrement up to 44% compared to R-UHPC.

It is noted that it was not possible to estimate both d_y and d_u due to the highly irregular behaviour of the RC curve, which is characterized by a peak near d_c followed by a significant drop in resistance. This is associated with widening the major crack and losing the concrete's contribution to resistance. The remaining portion of the curve essentially reflects the response of the steel reinforcement and, therefore, cannot be considered an estimate of the properties of the RC link slab but rather of the steel reinforcement itself.

When comparing specimens on average with R-UHPC and O-UHPC with 2% V_f of fibres, an improvement is observed in both ultimate displacements and ductility. The ultimate displacements improves by about 17%, while the displacements at yielding, peak, and ultimate stages increase by approximately 8%, 14%, and 21%, respectively. However, the increase in stiffness is limited to about 8%.

Table 12
Characteristic parameters of the force–displacement curves: d_c is the first-cracking displacement, d_y the yielding displacement and d_u the ultimate displacement, F_u the maximum force and K_f the secant stiffness.

Test label	d_c [mm]	d_y [mm]	d_u [mm]	F_u [kN]	K_f [kN/mm]
O-UHPC-V_f-1%	1.16	5.9	8.57	87	43.77
O-UHPC-V_f-2%	2.07	7.81	16.2	126	46.43
O-UHPC-V_f-3%	2.47	11.7	18.1	145	47.9
R-UHPC-V_f-2%	1.3	7.2	14.1	107	42.74
RC	0.52	–	–	35	29.55

Regarding the volumetric fraction of fibres, increasing from 1% to 2% in specimens with oriented fibres increases ultimate bending strength of about 30%, with an increase in all displacement thresholds, especially the peak displacement. On the other hand, increasing from 2% to 3%, a further increase in ultimate displacements is observed but much smaller, at around 13%, and in terms of ductility, the improvements are around 20%. Regarding stiffness, an increase of about 8% is noted. Interestingly, while V_f determines an almost linear increase in mechanical properties for UHPC specimens, in the case of link slabs, there is a sort of saturation and non-linear trend with very modest improvements when increasing from 2% to 3%.

Table 13 provides the information needed to characterize the crack patterns shown in Fig. 23. The table presents the number of cracks as well as the average crack characteristics. The most evident difference between the tested specimens is the number of cracks that is significantly larger in UHPC compared to RC, and increases for larger values of fibre volume. Also the fibre orientation leads to a limited increase in the number of cracks. Specifically, the number of cracks is approximately 8 in the RC specimen, 65 in the R-UHPC specimen with 2% V_f, and respectively 42, 83, and 116 in O-UHPC specimens with increasing fibre percentages. In general, the extent and width of the cracks in UHPC specimens tend to decrease compared to

Table 13

Main characteristics of the surface cracks on the tested specimens.

Test label	Crack distribution range [cm]	Number of cracks	Average crack spacing [mm]	Average crack width [mm]
O-UHPC-V_f-1%	−30 30	42	14.3	0.17
O-UHPC-V_f-2%	−40 40	83	9.6	0.11
O-UHPC-V_f-3%	−50 50	116	8.6	0.08
R-UHPC-V_f-2%	−30 30	65	9.2	0.19
RC	−30 30	8	75	0.42

reinforced concrete. Focusing on the UHPC specimens, the analysis of Table 13 reveals that the crack features are particularly sensitive to the volume fraction of fibres. Increasing the fibre volume consistently affects the crack distribution, number, length, and width, generally resulting in the improvement of the material performance in terms of crack management. However, beyond V_f 2%, there is no significant reduction in crack width, but only an increase in their number. The fibre orientation also affects the characteristics of the cracks and in particular their distribution. However, the variations in the cracking (R-UHPC-V_f-2% vs. O-UHPC-V_f-2%) are not as consistent as those observed with changes in fibre volume.

Steel fibres oriented in the matrix can effectively transfer interface shear stresses and mitigate stress concentration at weaker points, thus enhancing the initial crack resistance. Concurrently, the UHPC matrix, with its higher strength and stiffness, contributes to improving the bending stiffness (K_f). As the volumetric fibre fraction increases, the crack distribution range in O-UHPC specimens expands, suggesting that a larger V_f leads to an enlarged negative bending moment zone in the specimen. During the cracking stage, the steel fibres optimally transfer tensile stresses to uncracked sections, enhancing the specimen's crack resistance. The tensile strength and stiffness of UHPC make initial crack formation more challenging. Once cracked, the directionally oriented steel fibres leverage their bridging effect, resulting in a more uniform tensile stress distribution across the section and reducing stress concentration at crack tips. This significantly mitigates crack propagation and substantially boosts the post-cracking strength of the specimen. Therefore, UHPC link slabs with directionally oriented steel fibres exhibit superior crack resistance to those with randomly oriented fibres.

According to [89], under Service Load States (SLS), the maximum crack width in concrete structures should not exceed 0.2 mm. It must be verified that the rotation angle (θ) corresponding to a crack width of 0.2 mm is greater than the code limit (θ_{ST}). This indicates that a larger rotation of the link slab, compared to the minimum specified by the code, is necessary to reach the critical crack width.

$$\theta \geq \theta_{ST} \tag{4}$$

The rotation angle (θ) in O-UHPC specimens with varying V_f and RC specimens differs from θ values prescribed in various standards. The rotation angles for O-UHPC-V_f-1%, O-UHPC-V_f-2%, and O-UHPC-V_f-3% specimens, when crack width reaches 0.2 mm, are 0.00569 rad, 0.0063 rad, and 0.00844 rad, respectively. Hence, all test specimens meet the θ limits for both SLS (0.00161 rad) and Ultimate Load States (ULS) (0.00326 rad), as well as the American AASHTO standard [102] (0.00375 rad) and the Highway Bridge Regulations [89] (0.005 rad). The θ corresponding to a crack width of 0.2 mm in RC specimens is 0.00132 rad, which does not satisfy these θ limits. This suggests that RC specimens likely exhibit cracking under SLS, impacting their normal function and durability. Such considerations are summarized in Table 14.

4.3. Mechanics-based interpretative model

The authors have developed an interpretative mechanical model for the experimental results. Accurately predicting the ultimate bending strength of this system is complex because, despite its use of a statically determinate four-point bending scheme, the system is internally hyperstatic. This hyperstatic nature prevents the determination of the exact forces exchanged between the slab and the beam segments based solely on equilibrium, even with the presence of a debonding layer that may reduce these forces. It is important to note that the beam segments are significantly stiffer than the slab and are only permitted to rotate relative to the support. As a result, under these constrained conditions, the slab experiences primarily tensile deformations. In the configuration considered, where the height of the lever arm that the link slab can exert is much greater than the thickness of the slab, the longitudinal deformation of the slab is predominantly uniform in nature.

The exchanged forces at failure can be represented as shown in Fig. 24 with a simplified scheme. The rotational equilibrium about the pole O can be written as follows:

$$F \cdot x = F_t \cdot h \rightarrow F = F_t \cdot \frac{h}{x} \tag{5}$$

where F is the force applied by the actuator, F_t is the tensile capacity of the slab, and x and h are the respective lever arms defined in Fig. 24(b). The tensile ultimate capacity of the slab is theoretically the sum of the contributions from steel and concrete, as shown below:

$$F_t = A_c \cdot f_{tc} + A_s \cdot f_y = F_c + F_s \tag{6}$$

where A_c and A_s are the areas of concrete and steel respectively, and f_{tc} and f_y are their corresponding strengths.

However, it has been experimentally observed that even a small curvature of the slab, due to the rotation of the bridge segment, triggers the initiation of cracks in the extrados zone. These propagate to the barycentric reinforcement, where the reinforcement prevents further crack propagation. However, in UHPC it has been seen that the maximum force is reached when the tensile resistance in the superior zone is achieved. In contrast, in RC link slabs, the brittle tensile behaviour causes the entire thickness of the slab to be involved in the tensile ultimate capacity. Therefore, in calculating the resistance of the slab, it is important to use an effective thickness, approximately equal to the thickness of the extrados zone up to the barycentric reinforcements in the UHPC slab, and the entire thickness in the RC slab.

It has also been observed from the strain gauges on the steel reinforcement that, at the peak of force and associated deformation, the contribution of the steel is negligible. Therefore, for a simplified but possibly accurate estimate of the ultimate bending strength of the slab, it is appropriate to consider only the contribution of the concrete, as shown below.

$$F_t \approx A_{c,eff} \cdot f_{tc} = w \cdot t_{eff} \cdot f_{tc} \tag{7}$$

where t_{eff} is the effective thickness of the slab and w its width. Table 15 presents the results of the calculation of the ultimate bending capacity according to Eq. (5), using the expression in Eq. (7) for assessing the ultimate tensile capacity of the slab.

At failure, the simplified model demonstrates remarkable accuracy despite its simplicity, as illustrated in Table 16.

For link slabs with fibres oriented according to isostatic lines, the errors are small, approximately 1%, 4%, and 14% for V_f values of 1%, 2%, and 3%, respectively. The increase in error with volume fraction can be linked to the fact that while in the case of specimens subjected to tension the increase in tensile strength grows linearly, in the static scheme considered, the occurrence of unintended bending moments alters the behaviour of the isostatics and reduces the effectiveness of the additional fibre reinforcement. This is evident for the case with randomly oriented fibres, where the largest error is observed. The model tends to underestimate the ultimate bending capacity by 37%, which may also be due to an underestimation of the tensile strength of the concrete with randomly oriented fibres. For the case of plain concrete, the prediction is extremely accurate with an error of 3%. If the authors had included the contribution of steel in the calculation, they would

Table 14
Comparison of rotation angles (θ) according to various standards and different specimens (at crack width of 0.2 mm).

Specimen label	θ (rad)	Standard Limits (rad)			
		SLS [103]	ULS [103]	AASHTO [102]	JTG3362-2018 [89]
O-UHPC-V_f-1%	0.00569	0.00161	0.00326	0.00375	0.005
O-UHPC-V_f-2%	0.0063				
O-UHPC-V_f-3%	0.00844				
RC	0.00132				

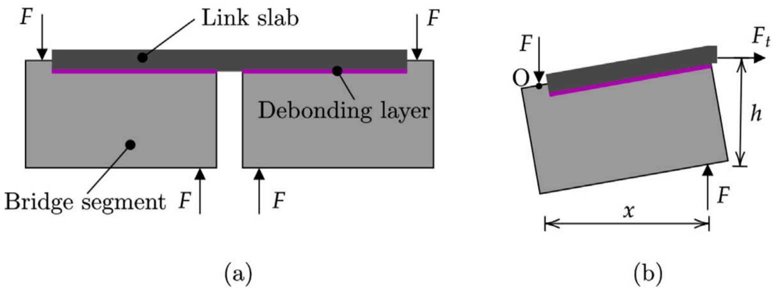

Fig. 24. Illustration of the explanatory mechanics-based model.

Table 15
Estimation of the ultimate bending capacity of the structural assembly with the link slab. w is the width of the link spab, t_{eff} the effective thickness, f_{tc} the tensile strength of concrete, h and x the lever arms defined in Fig. 24, and F_u the estimated ultimate force.

Label	w [mm]	t_{eff} [mm]	f_{tc} [MPa]	h [mm]	x [mm]	F_u Sim. [kN]
O-UHPC-V_f-1%	890	40	6.93	300	840	88
O-UHPC-V_f-2%			9.57			122
O-UHPC-V_f-3%			13.24			168
R-UHPC-V_f-2%			6.13			78
RC		100	1.13			36

Table 16
Experimental vs. simulated ultimate bending capacity of the structural assembly with the link slab.

Label	F_u Exp. [kN]	F_u Sim. [kN]	Relative error [%]
O-UHPC-V_f-1%	87	88	−1.26%
O-UHPC-V_f-2%	126	122	3.55%
O-UHPC-V_f-3%	145	168	−13.86%
R-UHPC-V_f-2%	107	78	37.29%
RC	35	36	−2.56%

have observed an error greater than 100%. The tensile contribution of steel is indeed 283 kN. In conclusion, the proposed mechanical model, despite its simplicity, can efficiently estimate the scale of the ultimate bending capacity with an average relative error of 5% for the considered cases. The authors have not verified the effectiveness of the model on experimental results involving the modification of the geometry, because the effects of the bolt distance from the edge and the absence of the debonding layer are difficult to quantify with such a simplified model.

5. Conclusions

The main novelty of the paper is the extensive and detailed mechanical characterization of 9 typologies of prefabricated UHPC link slabs. In particular, the novel results of this study can be summarized based on the parameters varied in the analysis:

- Bolt Edge Distance: Increasing the edge distance of the connectors in the prefabricated link slab from 100 to 400 mm progressively reduces the strength and ductility of the link slab by nearly 20% at each 100 mm step. A distance of 100 mm is optimal.
- Presence of a 5 mm Unbonded Layer: Link slabs ensure structural continuity between two decks without altering their static scheme. However, it is recommended to include an unbonded layer in the link slab to prevent direct contact with the beam, as friction can reduce the ultimate bending strength to distribute tensile stresses. The absence of this 5 mm gap leads to an approximate 18% ultimate bending strength reduction.
- UHPC with Randomly Oriented or Oriented fibres: The effect of fibre orientation along principal tensile stress directions, compared to randomly oriented fibres in link slabs, was quantified. In the case of casting with oriented channels, an increase in the ultimate force by about 17% was observed. The displacement at first cracking was reduced by 60%, and at yielding and ultimate by about 10%.
- Effect of fibre Volume Content in Oriented fibre UHPC: The impact of 1%, 2%, and 3% fibre volume content was evaluated. The ultimate bending capacity increased by about 30% from 1% to 2% and about 13% from 2% to 3%, indicating a saturation point beyond certain quantities. Conversely, the tensile strength increment was almost linear for the same variations in dog-bone tensile specimens, around 38% from 1% to 2% V_f and 2% to 3% V_f.

As previously noted in the literature, it was confirmed that using RC for link slabs leads to a 200% reduction in the ultimate bending strength compared to UHPC with 2% fibres and a 150% decrease in displacement at first cracking. It is interesting to note that all these variables do not significantly influence the stiffness. Considering consecutive variations of a given parameter, geometric or material, the variation never exceeded 10%.

In conclusion, the following constructive considerations are recommended: always ensure even a small unbonded layer of 5 mm to exploit the capabilities of UHPC link slabs. Moreover, the bolts should be distanced from the edge of nearly 100 mm. It is recommended to use oriented fibres in UHPC, easily obtained in prefabrication with oriented channels, as they provide an approximate 20% improvement. Increasing the fibre volume beyond 2% does not offer significant mechanical advantages and makes processing more difficult.

Future work will aim to develop predictive numerical models of the response to extend the experimental results to a broader range of parameters. The exploration of fatigue behaviour of UHPC link slabs will also be the object of future investigations.

CRediT authorship contribution statement

Junqing Xue: Writing – review & editing, Writing – original draft, Visualization, Validation, Supervision, Software, Resources, Project administration, Methodology, Investigation, Funding acquisition, Formal analysis, Data curation, Conceptualization. **Shengrong Mao:** Writing – original draft, Visualization, Methodology, Investigation, Formal analysis, Data curation. **Wei Xu:** Visualization, Validation, Methodology, Investigation, Formal analysis, Data curation. **Angelo Aloisio:** Writing – review & editing, Writing – original draft, Visualization, Validation, Methodology, Investigation, Formal analysis, Data curation, Conceptualization. **Yang Zhengxian:** Writing – review & editing, Writing – original draft, Visualization, Validation, Supervision, Software, Methodology, Investigation, Formal analysis, Data curation, Conceptualization. **Alessandro Contento:** Writing – review & editing, Visualization, Validation, Supervision, Methodology, Investigation, Formal analysis, Data curation. **Bruno Briseghella:** Writing – review & editing, Visualization, Validation, Supervision, Resources, Project administration, Methodology, Investigation, Funding acquisition, Formal analysis, Conceptualization.

Declaration of competing interest

All authors have participated in (a) conception and design, or analysis and interpretation of the data; (b) drafting the article or revising it critically for important intellectual content; and (c) approval of the final version.

This manuscript has not been submitted to, nor is under review at, another journal or other publishing venue.

The authors have no affiliation with any organization with a direct or indirect financial interest in the subject matter discussed in the manuscript

Acknowledgements

The research in this paper was sponsored by the National Natural Science Foundation of China (Grant Nos. 51508103, W2433120 and 51778148), the 2023 Fujian Provincial Transportation Science and Technology Demonstration Project (SF20230202), the Open Project Fund of the Sustainable and Innovative Bridge Engineering Research Center of Fujian Province University (Grant No. SIBERC 202203), the Open Project of Fujian Provincial Key Laboratory on Multi-Disasters Prevention and Mitigation in Civil Engineering (MPMC-2022-4) and the Recruitment Program of Global Experts Foundation (TM2012-27).

Data availability

Data will be made available on request.

References

[1] Shafei B, Alipour A, Shinozuka M. Prediction of corrosion initiation in reinforced concrete members subjected to environmental stressors: A finite-element framework. Cem Concr Res 2012;42(2):365–76. http://dx.doi.org/10.1016/j.cemconres.2011.11.001, cited By 83.
[2] Shafei B, Alipour A, Shinozuka M. A stochastic computational framework to investigate the initial stage of corrosion in reinforced concrete superstructures. Comput-Aided Civ Infrastruct Eng 2013;28(7):482–94. http://dx.doi.org/10.1111/mice.12019, cited By 38.
[3] Hajilar S, Shafei B. Atomic-scale investigation of physical adsorption of water molecules and aggressive ions to ettringite's surfaces. J Colloid Interface Sci 2018;513:104–16. http://dx.doi.org/10.1016/j.jcis.2017.09.019, cited By 25.
[4] Hajilar S, Shafei B. Structure, orientation, and dynamics of water-soluble ions adsorbed to basal surfaces of calcium monosulfoaluminate hydrates. Phys Chem Chem Phys 2018;20(38):24681–94. http://dx.doi.org/10.1039/c8cp03872d, cited By 24.
[5] Lima JM, de Brito J. Inspection survey of 150 expansion joints in road bridges. Eng Struct 2009;31(5):1077–84.
[6] Chen B, Zhuang Y, Huang F. Bridges without expansion joints. Beijing: People's Transportation Publishing House; 2019.
[7] Hulsey JL. Bridge lengths: jointless prestressed girder bridges. Tech. rep., Fairbanks, AK: Transportation Research Center, Institute of Northern Engineering, University of Alaska; 1992.
[8] Alampalli S, Yannotti A. In-service performance of integral bridges and jointless decks. Transp Res Rec 1998;(1624):1–7. http://dx.doi.org/10.3141/1624-01, cited By 37.
[9] Zuk W. Jointless bridges. In: Final report. 1981, Jointless Bridges Cited By 5.
[10] Loveall CL. Jointless bridge decks. Civ Eng New York, N.Y. 1985;55(11):64–7, cited By 15.
[11] Wasserman EP. Jointless bridge decks. Eng J 1987;24(3):93–100, cited By 18.
[12] Oesterle R, Glikin J, Larson S. Design of precast prestressed bridge girders made continuous. In: NCHRP report 322. 1989, Cited By 33.
[13] Burke Jr M. Integral bridges: Attributes and limitations. In: ACI national concrete engineering conference. 1992, Cited By 5.
[14] Burke Jr MP. Semi-integral bridges: movements and forces. Transp Res Rec 1994;(1460):1–7, cited By 29.
[15] Aloisio A, Pelliciari M, Xue J, Fragiacomo M, Briseghella B. Effect of pre-hole filled with high-damping material on the inelastic response spectrum of integral abutment bridges. J Earthq Eng 2023;27(12):3319–40.
[16] Fu R-H, Briseghella B, Xue J-Q, Aloisio A, Lin Y-B, Nuti C. Experimental and finite element analyses of laterally loaded rc piles with pre-hole filled by various filling materials in iabs. Eng Struct 2022;272:114991.
[17] Xue J, Aloisio A, Lin Y, Fragiacomo M, Briseghella B. Optimum design of piles with pre-hole filled with high-damping material: Experimental tests and analytical modeling. Soil Dyn Earthq Eng 2021;151:106995.
[18] Aloisio A, Contento A, Xue J, Fu R, Fragiacomo M, Briseghella B. Probabilistic formulation for the q-factor of piles with damping pre-hole. Bull Earthq Eng 2023;21(8):3749–75.
[19] Xue J, Briseghella B, Lin J, Huang F, Chen B. Design and field tests of a deck-extension bridge with small box girder. J Traffic Transp Eng (Engl Ed) 2018;5(6):467–79.
[20] Lin J, Briseghella B, Xue J, Tabatabai H, Huang F, Chen B. Temperature monitoring and response of deck-extension side-by-side box girder bridges. J Perform Constr Facil 2020;34(2):04019122.
[21] Gastal F, Zia P. Analysis of bridge beams with jointless decks. In: Proc. international association for bridge and structural engineering (IABSE) symp.. 1989, p. 555–60, Cited By 6.
[22] Zia P, Caner A, El-Safty A. Jointless bridge decks. Jointless Bridge Decks 1995;1–117, Cited By 27.
[23] Caner A, Zia P. Behavior and design of link slabs for jointless bridge decks. PCI J 1998;43(3):68–78. http://dx.doi.org/10.15554/pcij.05011998.68.80, cited By 101.
[24] U. E. Aktan H, Attanayake U. Combining link slab, deck sliding over backwall, and revising bearings. Bridge Decks; 2008.
[25] Caner A ZPZ. Behavior and design of link slabs for jointless bridge decks. PCI J 1998;43:68–78.
[26] Lu E. Calculation and analysis of the structure of continuously paved layers at the end of simply supported beam bridge deck. Theor Res Urban Constr 2015;32(5):2015N4980, (in Chinese).
[27] Alampalli S YA. In-service performance of integral bridges and jointless decks. Transp Res Rec 1998;1624:1–7.
[28] Liu H Y LL, Zhao SC. Study on bridge deck link slabs of simply supported girder bridges. Adv Mater Res 2014;1079–1080:280–5.
[29] Wing K, Kowalsky M. Behavior, analysis, and design of an instrumented link slab bridge. J Bridge Eng 2005;10(3):331–44. http://dx.doi.org/10.1061/(ASCE)1084-0702(2005)10:3(331), cited By 23.
[30] Li V, Lepech M, Li M. Field demonstration of durable link slabs for jointless bridge decks based on strain-hardening cementitious composites. In: Field demonstration of durable link slabs for jointless bridge decks based on strain-hardening cementitious composites. 2005, p. 1–147, Cited By 34.

[31] Lepech M, Li V. Application of ecc for bridge deck link slabs. Mater Struct/Mater Constr 2009;42(9):1185–95. http://dx.doi.org/10.1617/s11527-009-9544-5, cited By 258.
[32] Samani G. Structural performance of link slabs subjected to monotonic and fatigue loading incorporating engineered cementitious composites (M.S. thesis), 2013, Cited By 3.
[33] Xiong L. Research on ecc deck connection plates in simply supported beam bridges (Ph.D. thesis), Southeast University, Nanjing; 2017.
[34] Lepech M D LVC. Application of ecc for bridge deck link slabs (conference paper). Mater Struct/Mater Constr 2009;42:1185–95.
[35] Royce M. Utilization of ultra-high performanc concrete (uhpc) in new york. 2016, Cited By 1.
[36] Karim R, Najimi M, Shafei B. Assessment of transport properties, volume stability, and frost resistance of non-proprietary ultra-high performance concrete. Constr Build Mater 2019;227. http://dx.doi.org/10.1016/j.conbuildmat.2019.117031, cited By 43.
[37] Shi W, Shafei B, Liu Z, Phares B. Early-age performance of longitudinal bridge joints made with shrinkage-compensating cement concrete. Eng Struct 2019;197. http://dx.doi.org/10.1016/j.engstruct.2019.109391, cited By 18.
[38] Shi W, Shafei B, Liu Z, Phares B. Longitudinal box-beam bridge joints under monotonic and cyclic loads. Eng Struct 2020;220. http://dx.doi.org/10.1016/j.engstruct.2020.110976, cited By 5.
[39] Dopko M, Najimi M, Shafei B, Wang X, Taylor P, Phares B. Flexural performance evaluation of fiber-reinforced concrete incorporating multiple macro-synthetic fibers. Transp Res Rec 2018;2672(27):1–12. http://dx.doi.org/10.1177/0361198118798986, cited By 26.
[40] Dopko M, Najimi M, Shafei B, Wang X, Taylor P, Phares B. Strength and crack resistance of carbon microfiber reinforced concrete. ACI Mater J 2020;117(2):11–23. http://dx.doi.org/10.14359/51720297, cited By 19.
[41] Wang Liming GH, Weizhong Tang. Application of polypropylene fiber concrete in continuous deck and expansion joints of bridges. J North Forest Univ 2003;31:49–50.
[42] Haikal G, Ramirez JA, Jahanshahi MR, Villamizar S, Abdelaleim O. Link slab details and materials. 2019.
[43] Graybeal B. Design and construction of field-cast uhpc connections. Tech. Rep., USA: FHWA; 2014, FHWA-HRT-14-084.
[44] Graybeal B, Brühwiler E, Kim B, et al. International perspective on uhpc in bridge engineering. J Bridge Eng 2020;25(11):04020094.
[45] Graybeal B. Emerging uhpc-based bridge construction and preservation solutions. In: Symposium on ultra-high performance fibre-reinforced concrete. Paris: RILEM; 2017, p. 965–74.
[46] Doiron G, White P. Uhpc link slab solutions in north america. In: Symposium on ultra-high performance fibre-reinforced concrete. Paris: RILEM; 2017, p. 975–82.
[47] Graybeal B. Design and construction of field-cast uhpc connections. Tech. Rep., USA: FHWA; 2019, FHWA-HRT-19-011.
[48] Li N. Performance of link slab using ecc and uhpc, D. Maryland, USA: University of Maryland; 2019.
[49] Lin J, Briseghella B, Xue J, Pan X. Research on flexural performance and crack width calculation method of ultra-high performance concrete link slab. Bridge Constr 2022;52(5):60–8.
[50] Cameron J. Engineered fiber reinforced concrete systems for bridge deck link slab applications. Eng Fibre-reinforced Concr Syst Bridge Deck Link Slab Appl 2014. Cited By 2.
[51] Xiangfeng P. Experimental study on the mechanical performance of ultra high performance concrete continuous deck slabs (Ph.D. thesis), Fuzhou: Fuzhou University; 2019.
[52] Zhenguo Y. Research on the mechanical performance of uhpc connection plate-backwall structure at bridge abutments (Ph.D. thesis), Fuzhou: Fuzhou University; 2021.
[53] Wei X. Research on the mechanical properties of prefabricated uhpc connection plates (Ph.D. thesis), Fuzhou: Fuzhou University; 2022.
[54] Benmokrane B, El-Salakawy E, El-Ragaby A, Lackey T. Designing and testing of concrete bridge decks reinforced with glass frp bars. J Bridge Eng 2006;11(2):217–29. http://dx.doi.org/10.1061/(ASCE)1084-0702(2006)11:2(217), cited By 156.
[55] Benmokrane B, El-Salakawy E, El-Gamal S, Goulet S. Construction and testing of an innovative concrete bridge deck totally reinforced with glass frp bars: Val-alain bridge on highway 20 east. J Bridge Eng 2007;12(5):632–45. http://dx.doi.org/10.1061/(ASCE)1084-0702(2007)12:5(632), cited By 82.
[56] Arafa A, Farghaly A, Ahmed E, Benmokrane B. Laboratory testing of gfrp-rc panels with uhpfrc joints of the nipigon river cable-stayed bridge in northwest Ontario, Canada. J Bridge Eng 2016;21(11). http://dx.doi.org/10.1061/(ASCE)BE.1943-5592.0000943, cited By 40.
[57] Ahmed E, Settecasi F, Benmokrane B. Construction and testing of gfrp steel hybrid-reinforced concrete bridge-deck slabs of sainte-catherine overpass bridges. J Bridge Eng 2014;19(6). http://dx.doi.org/10.1061/(ASCE)BE.1943-5592.0000581, cited By 30.
[58] Saini D, Shafei B. Investigation of concrete-filled steel tube beams strengthened with cfrp against impact loads. Compos Struct 2019;208:744–57. http://dx.doi.org/10.1016/j.compstruct.2018.09.057, cited By 54.
[59] Abdelkarim O, Ahmed E, Benmokrane B, Loranger M-A. Design and field testing of a first continuous slab-on-girder bridge with a hybrid gfrp-steel-reinforced bridge deck in Canada. J Bridge Eng 2020;25(8). http://dx.doi.org/10.1061/(ASCE)BE.1943-5592.0001579, cited By 6.
[60] Ryes J, Robertson I. Precast link slabs for jointless bridge decks. Precast Link Slabs Jointless Bridge Decks 2011. Cited By 3.
[61] Lárusson L. Development of flexible link slabs using ductile fiber reinforced concrete. Dev Flex Link Slabs using Ductile Fiber Reinforced Concr 2013. Cited By 10.
[62] Xue J, Briseghella B, Huang F, Nuti C, Tabatabai H, Chen B. Review of ultra-high performance concrete and its application in bridge engineering. Constr Build Mater 2020;260:119844.
[63] Wang Dehui WL, Caijun Shi. Research and application of ultra high performance concrete in China. Bull Silic 2016;35:141–9.
[64] M R. Utilization of ultra-high performance concrete (uhpc) in New York. 2016.
[65] Teng L, Meng W, Khayat K. Rheology control of ultra-high-performance concrete made with different fiber contents. Cem Concr Res 2020;138:106222.
[66] Qiu M, Zhang Y, Qu S, Zhu Y, Shao X. Effect of reinforcement ratio, fiber orientation, and fiber chemical treatment on the direct tension behavior of rebar-reinforced uhpc. Constr Build Mater 2020;256.
[67] Maya Duque LF, Graybeal B. Fiber orientation distribution and tensile mechanical response in uhpfrc. Mater Struct 2017;50:1–17.
[68] Abrishambaf A, Pimentel M, Nunes S. Influence of fibre orientation on the tensile behaviour of ultra-high performance fibre reinforced cementitious composites. Cem Concr Res 2017;97:28–40.
[69] Wang D, Shi C, Wu L. Research and application of ultra high performance concrete in China. Bull Silic 2016;35:141–9.
[70] Wang Q, Guo Z. Application of uhpc steel fiber oriented arrangement spreader in steel deck pavement. Constr Technol 2021;50:81–4.
[71] Walsh K, Hicks N, Steinberg E, Hussein H, Semendary A. Fiber orientation in ultra-high-performance concrete shear keys of adjacent-box-beam bridges. ACI Mater J 2018;115(2):227–38.
[72] Shao X, Zhou Y, Cao J, Sun P, Zhu F. Experimental study on flexural behavior of novel continuous deck structure in steel simply-supported beams. China Civ Eng J 2019;52:80–92.
[73] Ataei A, Bradford MA, Liu X. Experimental study of composite beams having a precast geopolymer concrete slab and deconstructable bolted shear connectors. Eng Struct 2016;114:1–13.
[74] Pavlović M, Marković Z, Veljković M, et al. Bolted shear connectors vs. headed studs behaviour in push-out tests. J Constr Steel Res 2013;88:134–49.
[75] Du H, Zhang B, Hu X, Kou L, Xia Y. Experimental study on shear behavior of bolt connectors in steel-concrete composite beams. J Build Struct 2017;38:308–14.
[76] Chen Y, Zhao Y, West J, et al. Behaviour of steel-precast composite girders with through-bolt shear connectors under static loading. J Constr Steel Res 2014;103:168–78.
[77] Liu Z. Experimental study on shear performance of high-strength bolt connectors in prefabricated composite beams (Ph.D. thesis), Xiangtan University, Xiangtan; 2017.
[78] Briseghella B, Xu W, Xue J-Q, Lin J-H, Nuti C, et al. Numerical analyses on flexural performance of prefabricated uhpc link slab. In: IABSE congress, ghent 2021: structural engineering for future societal needs. IABSE, International Association for Bridge and Structural Engineering; 2021, p. 801–8.
[79] Chen B, Huang F, Xue J, et al. Review on research of jointless bridges. J Transp Eng 2022;22:1–40.
[80] Chen B, Fu C, Zhuang Y, et al. Current application and development strategies of jointless bridges in China. J China Foreign Highw 2018;38(1):87–95.
[81] Chen B, Wang C, Xue J, Huang F. Investigation and analysis of jointless bridges in China. J Archit Civ Eng 2022;9(5):13–21.
[82] Briseghella B, Tang Y, Xue J, Chen B, Huang F. Review of research on approach slabs in jointless bridges. J Fuzhou Univ (Nat Sci Ed) 2021;49(2):209–16.
[83] General code for design of highway bridges and culverts, standard code for highway bridges and culverts in China. Beijing, China: Ministry of Transport of the People's Republic of China; 2015.
[84] ASTM A490-18ae1. Standard specification for structural bolts, alloy steel, heat treated, 150 ksi minimum tensile strength. 2018, available online: https://www.astm.org/Standards/A490.htm.
[85] Xue JQ, Mao SR, Cacciola P, et al. Experimental evaluation of the effectiveness of fiber orientation methods on the mechanical performance of UHPFRC. Constr Build Mater 2024;448:138184.
[86] Kang ST, Lee BY, Kim J-K, Kim YY. The effect of fibre distribution characteristics on the flexural strength of steel fibre-reinforced ultra high strength concrete. Constr Build Mater 2011;25(5):2450–7.
[87] Wille K, Kim DJ, Naaman AE. Strain-hardening uhp-frc with low fiber contents. Mater Struct 2011;44:583–98.
[88] Huang H, Gao X, Teng L. Fiber alignment and its effect on mechanical properties of uhpc: An overview. Constr Build Mater 2021;296:123741.
[89] ISof the People's Republic of China. JTG3362-2018 specifications for design of highway reinforced concrete and prestressed concrete bridges and culverts. Beijing: China Communications Press; 2018.

[90] Su J, Ma X, Chen B, Sennah K. Full-scale bending test and parametric study on a 30-m span prestressed ultra-high performance concrete box girder. Struct Concr 2019;23(7):1276–89. http://dx.doi.org/10.1177/1369433219894244.

[91] Yang J, Chen B, Nuti C. Influence of steel fiber on compressive properties of ultra-high performance fiber-reinforced concrete. Constr Build Mater 2021;302:124104. http://dx.doi.org/10.1016/j.conbuildmat.2021.124104.

[92] Yang J, Chen B, Wu X, Xu G. Quantitative analysis of steel fibers on uhpfrc uniaxial tensile behavior using x-ct and utt. Constr Build Mater 2023;368:130349. http://dx.doi.org/10.1016/j.conbuildmat.2023.130349.

[93] Reactive powder concrete, standard GB/t 31387-2015, national standard of the People's Republic of China. General Administration of Quality Supervision, Inspection and Quarantine of the People's Republic of China; Standardization Administration of the People's Republic of China; 2015.

[94] Dragonfly: Advanced Imaging Analysis Software, https://www.theobjects.com/dragonfly.

[95] Oesch T, Landis E, Kuchma D. A methodology for quantifying the impact of casting procedure on anisotropy in fiber-reinforced concrete using X-ray CT. Mater. Struct. 2018;51:73. http://dx.doi.org/10.1617/s11527-018-1198-8.

[96] Standard test method for fiber reinforced concrete, construction industry standard CECS 13-2009. China Association for Engineering Construction Standardization; 2009.

[97] ASTM International. Standard test method for flexural performance of fiber-reinforced concrete (using beam with third-point loading). ASTM Standard; 2019, http://dx.doi.org/10.1520/C1609_C1609M-19A.

[98] Standard for test methods of concrete physical and mechanical properties, national standard GB/t 50081-2019. Ministry of Housing and Urban-Rural Development of the PRC; State Administration for Market Regulation; 2019.

[99] AQSIQ, SAC. Metallic materials - tensile testing - part 1: Method of test at room temperature, national standard GB/T 228.1-2010, implemented on december 1 2011, superseded by GB/T 228.1-2021. 2010.

[100] Rafiee A. Computer modeling and investigation on the steel corrosion in cracked ultrahigh performance concrete. Kassel: Kassel University Press; 2012.

[101] Makita T. Fatigue behaviour of UHPFRC and r-UHPFRC-RC composite members. EPLF, Lausanne; 2014.

[102] AASHTO. AASHTO LRFD bridge design specifications. Washington, USA: AASHTO; 2017.

[103] of Transport of the People's Republic of China Ministry. General specifications for design of highway bridges and culverts (JTG d60-2015). Beijing: China Communications Press; 2015.